Check for updates

Geophysical Research Letters

RESEARCH LETTER
10.1029/2025GL119307

Climate Change Alters Teleconnections

E. Vos[1], P. Huybers[2], and E. Tziperman[2]

[1]Laboratoire de Météorologie Dynamique/IPSL, Sorbonne Université, ENS, PSL Research University, Ecole Polytechnique, CNRS, Paris, France, [2]Department of Earth and Planetary Sciences and School of Engineering and Applied Sciences, Harvard University, Cambridge, MA, USA

Key Points:

- Anthropogenic climate change has altered large-scale climate teleconnections, affecting regional temperatures
- Changes to the teleconnections of El Niño-Southern Oscillation, the Indian Ocean Dipole, and Pacific Decadal Oscillation between 1960–1990 and 1990–2020 are robustly observed
- Future climate change is projected to further alter teleconnection patterns, amplifying their regional influence

Supporting Information:

Supporting Information may be found in the online version of this article.

Correspondence to:

E. Vos,
eran.vos@gmail.com

Citation:

Vos, E., Huybers, P., & Tziperman, E. (2026). Climate change alters teleconnections. *Geophysical Research Letters*, *53*, e2025GL119307. https://doi.org/10.1029/2025GL119307

Received 5 SEP 2025
Accepted 22 DEC 2025

Author Contributions:

Conceptualization: E. Vos, P. Huybers, E. Tziperman
Formal analysis: E. Vos
Investigation: E. Vos
Methodology: E. Vos, P. Huybers, E. Tziperman
Writing – original draft: E. Vos
Writing – review & editing: E. Vos, P. Huybers, E. Tziperman

© 2026. The Author(s).
This is an open access article under the terms of the Creative Commons Attribution-NonCommercial-NoDerivs License, which permits use and distribution in any medium, provided the original work is properly cited, the use is non-commercial and no modifications or adaptations are made.

Abstract Internal modes of climate variability, such as El Niño and the North Atlantic Oscillation (NAO), can have strong influences upon distant weather patterns, effects that are referred to as "teleconnections." The extent to which anthropogenic climate change has and will continue to affect these teleconnections, however, remains uncertain. Here, we employ a covariance fingerprinting approach to demonstrate that shifts in teleconnection patterns affecting monthly temperatures between the periods 1960–1990 and 1990–2020 are attributable to anthropogenic forcing. We further apply multilinear regression to assess the regional contributions and statistical significance of changes in five key climate modes: the El Niño-Southern Oscillation, NAO, Southern Annular Mode, Indian Ocean Dipole, and the Pacific Decadal Oscillation. In many regions, observed changes exceed what would be expected from natural variability alone, further implicating an anthropogenic influence. Finally, we provide projections of how these teleconnections will alter in response to further changes in climate.

Plain Language Summary Large-scale patterns in the climate system, such as El Niño and the North Atlantic Oscillation, can have strong influences upon distant weather patterns, effects that are referred to as "teleconnections." However, it is unclear to what degree anthropogenic climate change is altering these teleconnections. We show that shifts in these climate connections between 1960–1990 and 1990–2020 cannot be explained by natural variability alone and can be attributed to human influence. We examine five major climate modes and find that their effects on remote regional temperatures have already changed, impacting many parts of the world. Finally, we provide projections showing how these climate teleconnections are likely to further evolve in a warming future.

1. Introduction

Modes of internal variability such as the El Niño-Southern Oscillation (ENSO), North Atlantic Oscillation (NAO), Southern Annular Mode (SAM), Indian Ocean Dipole (IOD), and the Pacific Decadal Oscillation (PDO) are recurring large-scale oceanic and atmospheric patterns. These patterns influence local and remote temperatures, precipitation, and extreme weather events (Alexander et al., 2002; Casanueva et al., 2014; Casselman et al., 2023; Hobeichi et al., 2024; Karoly, 1989; Reboita et al., 2021; Simon Wang et al., 2015; Wallace & Gutzler, 1981; Wang & Schimel, 2003; Yeh et al., 2018) with significant environmental, social, and economic impacts (Hardiman et al., 2020; Kurths et al., 2019; Wang & Schimel, 2003; Zebiak et al., 2015). Projecting changes to the effects of these modes in a warmer future climate is critical for adaptation efforts (Gillett et al., 2003; King et al., 2010; Paeth & Pollinger, 2010).

Teleconnections are typically induced by atmospheric Rossby waves (Casselman et al., 2023; Hardiman et al., 2020; Hoskins & Karoly, 1981; Reboita et al., 2021) that are triggered by anomalies of sea surface temperature or surface heat fluxes, often via the mediation effects of atmospheric convection. The teleconnection pattern of a given variability mode (e.g., ENSO) can change between events because differences in the state of the ocean and atmosphere can affect wave propagation, including due to other modes that can exert a modulating effect on the teleconnections (Gershunov & Barnett, 1998; Hardiman et al., 2020; Joshi et al., 2021). Previous studies (Yeh et al., 2018) found indications of changes in teleconnection patterns since the 1990s, including in the effect of ENSO on North American precipitation (Simon Wang et al., 2015) and the effects of the Indian Ocean warming on the NAO (Hoerling et al., 2004). As climate change continues, such teleconnections may be further affected, as suggested for ENSO (Beverley et al., 2024; Lieber et al., 2024). Some modes and the relation between them may change in the future, as projected for the NAO and AO under extensive climate warming (Hamouda et al., 2021).

19448007, 2026, 2, Downloaded from https://agupubs.onlinelibrary.wiley.com/doi/10.1029/2025GL119307 by Weizmann Institute Of Science, Wiley Online Library on [15/01/2026]. See the Terms and Conditions (https://onlinelibrary.wiley.com/terms-and-conditions) on Wiley Online Library for rules of use; OA articles are governed by the applicable Creative Commons License

Observational analyses, detection–attribution studies, and climate model projections indicate that anthropogenic forcing is modifying not only the mean state of the climate system but also the structure, strength, and spatial patterns of climate teleconnections. Early attribution work emphasized that spatial patterns in the response to anthropogenic forcing are subject to substantial uncertainty (Jones et al., 2016), yet more recent studies show growing evidence that teleconnections are being reshaped by anthropogenic climate change (Bilbao et al., 2019; Deser et al., 2017). For example, changes in the Walker circulation and tropical convection under warming have already altered ENSO variability and its global teleconnections, with both historical amplification and robust end-of-century increases in ENSO-driven precipitation anomalies emerging across models (Cai et al., 2023; Power et al., 2013; Xie et al., 2010). Similarly, global-scale analyses demonstrate that warming reorganizes atmospheric bridges and storm-track pathways through which variability modes influence remote regions (Burke et al., 2017). Outside the tropics, Arctic amplification and sea-ice loss have been linked to the evolution of Arctic–midlatitude teleconnection pathways, with causal-network approaches revealing modified dynamical links between high-latitude variability, the polar vortex, and midlatitude circulation patterns in recent decades (Galytska et al., 2023). These studies suggest that anthropogenic forcing can influence both the amplitude and spatial expression of teleconnections, motivating a systematic evaluation of how forced changes compare to internal variability within the climate system.

Attribution of systematic shifts in global teleconnection patterns via covariance matrices of monthly mean temperature has not, to our knowledge, been addressed in the literature. Below, we first apply a covariance fingerprinting framework, projecting observed changes in temperature covariance onto model-simulated patterns of covariance change under greenhouse gas forcing. This approach allows us to formally attribute changes in global teleconnection structure to anthropogenic climate change. We later apply a second, complementary attribution approach that is based on a point-wise multilinear regression analysis.

2. Results

2.1. Global Analysis of Climate Change Impacts on Teleconnections of Internal Variability Modes

We first examine the change in global teleconnection patterns using the covariance matrix of monthly average temperature anomalies. Given T_i as the monthly temperature anomaly at grid point i, the covariance matrix is $C = \{c_{ij}\} = \langle T_i T_j \rangle$ where angle brackets indicate time averaging. Therefore, row i of the covariance matrix corresponds to the covariance of the monthly temperatures at the geographical location corresponding to this index with all other locations, and can be plotted as a map. We compose such covariance matrices of the monthly average temperature anomalies among all grid cells between 60°N and 60°S for the observations (Rohde & Hausfather, 2020) and the model control and historical runs (Danabasoglu et al., 2020; Kay et al., 2015) (see Methods). To visualize the covariance change, we plot maps of the temperature covariance during 1960–1990 and 1990–2020, as well as the difference between them in Figure 1 as follows. Note that the left and middle columns display most of the well-established teleconnections (discussed in Supporting Information S1), such as the positive correlation between ENSO and Australia. To focus on ENSO teleconnection changes, for example, we average the rows of the covariance matrix corresponding to all i points within the NINO3.4 region and plot the resulting average as a map. Similarly, the changes to the IOD and PDO teleconnections are depicted as appropriate averages over the corresponding regions, as discussed in the Methods section (Equation 3 in Supporting Information S1). For the effect of GMST, we average all rows, weighted by cosine latitude. Because the covariance fingerprint is constructed from surface temperature covariances, SAM and NAO are excluded. Note that changes in teleconnections may include spatial shifts, changes in frequencies, amplitude, or the relation between variability modes. Our focus here is on the changes to spatial patterns (of monthly temperatures) and their amplitude as seen through the covariance matrix.

Various changes in covariance are seen in the results plotted in the right column of Figure 1, which shows the difference between the periods of 1990–2020 and 1960–1990. For example, Figure 1f shows that ENSO teleconnections become stronger in Australia, as indicated by the red color there. Figures 1d and 1e show that when El Niño events occur, the monthly temperatures over Australia increase. The panels on the right hand side (e.g., Figure 1f) then show the change in the teleconnection. Teleconnection may change for two reasons. First, a change in the sensitivity to the remote influence, where a positive difference then implies that during the latter period, 1990–2020, the response of monthly temperatures to El Niño events is stronger than during the preceding period. Second, covariance differences that show an intensified pattern (e.g., for ENSO and Australia) could be

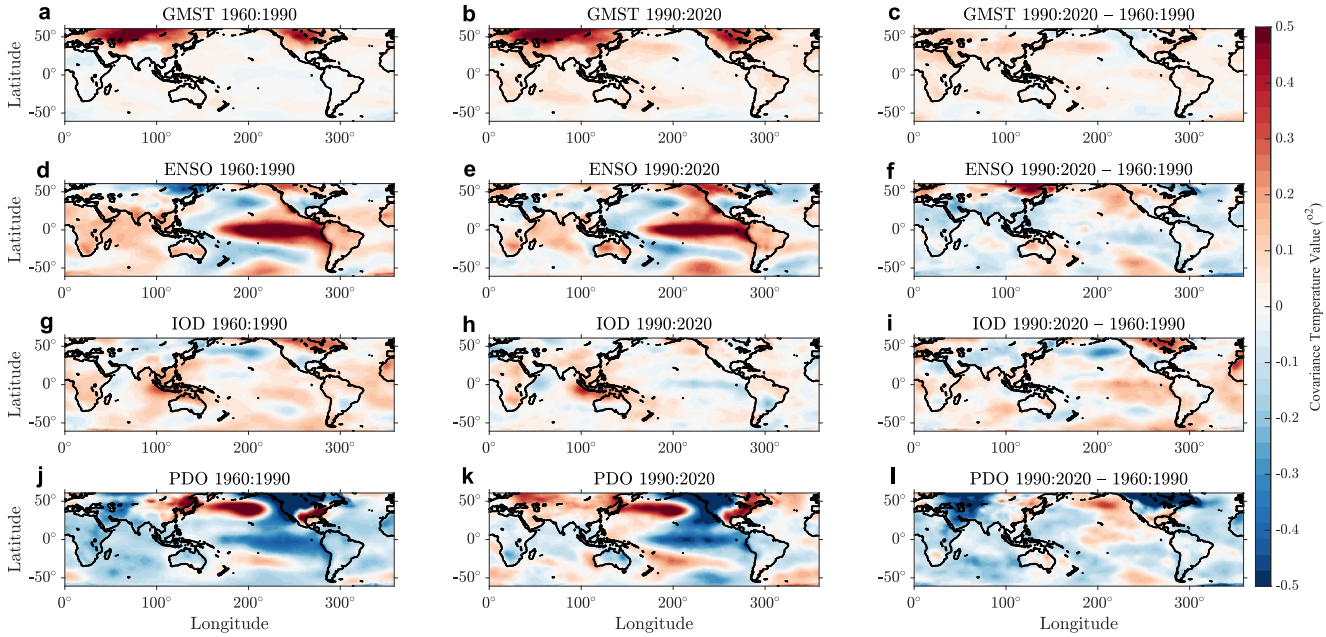

Figure 1. *Covariance changes across* 30*-year epochs*. The left column shows covariance averaged over all grid cells (top row), the Niño3.4 region (second row), the Indian Ocean Dipole region (third row), and the Pacific Decadal Oscillation (PDO) region (bottom row) for 1960–1990. The middle column is the same as the left column, but for the 1990–2020 period, and the right column shows the difference between the two periods. Note, the PDO covariance values in the bottom row are divided by 4 to facilitate the use of the same color range as the rest of the panels.

because ENSO variability itself increased. Covariance fingerprinting analyses do not separate between these two possible reasons for the change in teleconnection, but the regression analysis in the following section does provide this information, as discussed there.

In some cases, the sign of the ENSO teleconnection changes, which clearly implies a change in sensitivity. For example, temperatures switch from increasing with El Niño (positive teleconnection) to decreasing when El Niño occurs (negative) in Northeast Africa. ENSO teleconnection signs also switch over South Asia and Western Europe (Figure 1f).

To briefly review some other teleconnections changes, covariance with GMST shows increased warming over Africa, Asia, South America, and Eastern North America relative to other parts of the world (Figure 1c). For the IOD (Figures 1g–1i), we see a change in the amplitude and structure of teleconnections in Australia, Africa, Asia, and the Middle East. Finally, for the PDO (Figures 1j–1l), we observe a sign switch in Western Europe and Eastern North America, as well as a change in amplitude in Africa, Australia, and South America.

To test if changes in global teleconnection patterns are attributable to anthropogenic climate change, we use a covariance fingerprinting approach (see Methods) that is similar to the standard fingerprinting methods (Hasselmann, 1979; Hegerl et al., 1996; Ribes et al., 2009) but involves projecting the observed change in covariance onto that obtained from climate model simulations forced by historical changes in greenhouse gasses, aerosols, land use, and solar variability. We calculate a scalar measure of this projection, referred to as S_{obs},

$$S^{\text{obs}} = \frac{\left\langle \Delta C^{\text{obs}}, \Delta C^{\text{model}}_{\text{forced}} \right\rangle_F}{\| \Delta C^{\text{model}}_{\text{forced}} \|^2_F}. \quad (1)$$

S quantifies how strongly the observed change in covariance projects onto the model's forced pattern of changes in covariance, normalized by the square of the latter. The subscript F refers to the Frobenius norm, or the square root of the sum of the squares of all elements. S inherently contains all modes, including GMST. Intuitively, if the covariance matrices are identical, $S = 1$. If they share the same sign pattern, S is larger than 0. Conversely, if the sign pattern is opposite, S becomes negative. Thus, S provides a scalar measure of the similarity between covariance matrices.

19448007, 2026, 2, Downloaded from https://agupubs.onlinelibrary.wiley.com/doi/10.1029/2025GL119307 by Weizmann Institute Of Science, Wiley Online Library on [15/01/2026]. See the Terms and Conditions (https://onlinelibrary.wiley.com/terms-and-conditions) on Wiley Online Library for rules of use; OA articles are governed by the applicable Creative Commons License

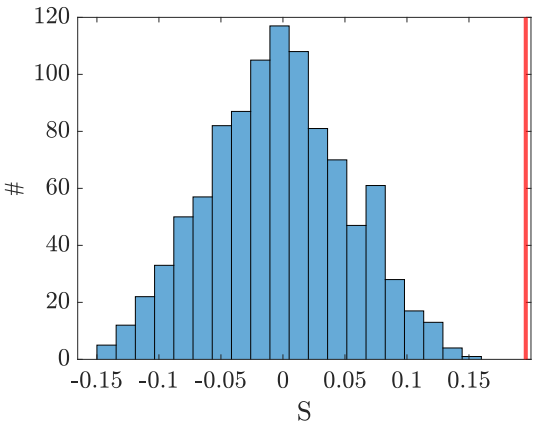

Figure 2. *Covariance fingerprint*. S_{obs} (red line) is larger than any of 1,000 realizations of S_{null} (histogram). S_{obs} is the observed covariance difference between 1960–1990 and 1990–2020 projected onto that produced by CESM2-LE historical runs. Each S_{null} realization is the same as S_{obs} but is computed using pairs of 30-year periods that are randomly drawn from the CESM2 long control run.

Figure 2 compares S_{obs} against 1,000 realizations of S_{null}, a covariance fingerprint calculated between randomly selected pairs of 30-year periods in the CESM2 control run (Danabasoglu et al., 2020; Kay et al., 2015). S_{null} samples random changes in covariance due to natural variability. We find that all realized values of S_{null} are smaller than S_{obs}. This calculation thus indicates that changes in global teleconnections are inconsistent with being solely the result of internal variability and, instead, are attributable to anthropogenic climate change.

The covariance fingerprinting method used here is a statistical analysis that tests for changes across all modes and locations and therefore captures the significance of the global change. It does not, however, provide regional specificity. The next section presents a complementary analysis that focuses on regional aspects.

2.2. Spatially Resolved Significance of Changes in Teleconnections

Using the covariance fingerprinting approach, we find that global teleconnection patterns changed between 1960–1990 and 1990–2020 in response to anthropogenic climate change. In this section, we complement the above global analysis by examining point-wise changes to teleconnections for GMST and each of the five modes: ENSO, NAO, SAM, PDO, and IOD. Note that we now include the NAO and SAM, whose indices are defined in reference to sea-level pressure patterns, as opposed to temperature patterns. Our approach is based on multilinear regression (Methods, Equation 4 in Supporting Information S1), which examines the differences between 1960–1990 and 1990–2020 in relation to anthropogenic climate change by comparing observations to a large ensemble of model results (Kay et al., 2015). To stabilize the multilinear regression, the modes are orthogonalized and standardized (see Methods).

Before proceeding to a point-wise attribution analysis of the difference between the two periods, we examine the contribution of each mode and GMST to monthly average global temperature anomalies over 1950–2020 (Figure SI1 in Supporting Information S1), finding well-known patterns that are listed explicitly in Supporting Information S1 (Anderson et al., 2017; Cai et al., 2011, 2020; Kumar et al., 2017; Linderholm et al., 2011; Roy et al., 2016; Saji et al., 2005; Sandler et al., 2024; Shi et al., 2019; Yang & DelSole, 2012; Zhou et al., 2024). Differences in regression coefficients between 1960–1990 and 1990–2020 are shown in Figure 3. The patterns of the temperature-based modes (GMST, ENSO, and IOD shown in Figures 3a, 3b, and 3f) share features in common with the covariance-based results (shown in Figures 1c, 1f, and 1i), with pattern correlations of 0.77, 0.98, and 0.59, respectively. In addition to the aforementioned changes in the response to GMST, we see strong Arctic amplification (Figure 3a), indicating a greater response of monthly temperatures in this region to GMST during recent decades. The regression approach, unlike covariance fingerprinting, however, shows that GMST is associated with the well-known cooling pattern in the East Pacific (Kosaka & Xie, 2013) and that ENSO is anti-correlation with Arctic temperatures. Differences arise between our two approaches because the regression-based approach isolates the component of temperature variability attributable to each mode after removing shared influences among GMST, ENSO, and IOD. In contrast, the covariance maps reflect the full co-variability between regional and base-region temperatures, including common signals from inter-mode correlations. Furthermore, the regression approach uses standardized amplitudes of each mode.

We focus on regions where changes in regression coefficients are statistically significant, as tested via bootstrapping (Figure SI4 in Supporting Information S1). These changes are not explained by internal variability in the CESM2 control run ($P < 0.05$, Figures SI4 and SI7 in Supporting Information S1) and are consistent with those found in the CESM2-LE historical runs ($P > 0.05$, Figure SI6 in Supporting Information S1). In general, 5% of grid points may be expected to pass a significance test at a 95% significance level. The fraction of grid points that pass, however, is significantly higher for GMST (28%), ENSO (20%), PDO (9.8%), and IOD (15%) teleconnection changes (Figure 3). Values are more comparable to those expected by chance for the NAO (3.4%) and SAM (4.0%), reflecting primarily that the observed changes do not correspond with those produced by the CESM2 historical run. Note that for the NAO and SAM, large portions of the domain do not show statistically significant differences between the two periods when evaluated against the bootstrapped data.

19448007, 2026, 2, Downloaded from https://agupubs.onlinelibrary.wiley.com/doi/10.1029/2025GL119307 by Weizmann Institute Of Science, Wiley Online Library on [15/01/2026]. See the Terms and Conditions (https://onlinelibrary.wiley.com/terms-and-conditions) on Wiley Online Library for rules of use; OA articles are governed by the applicable Creative Commons License

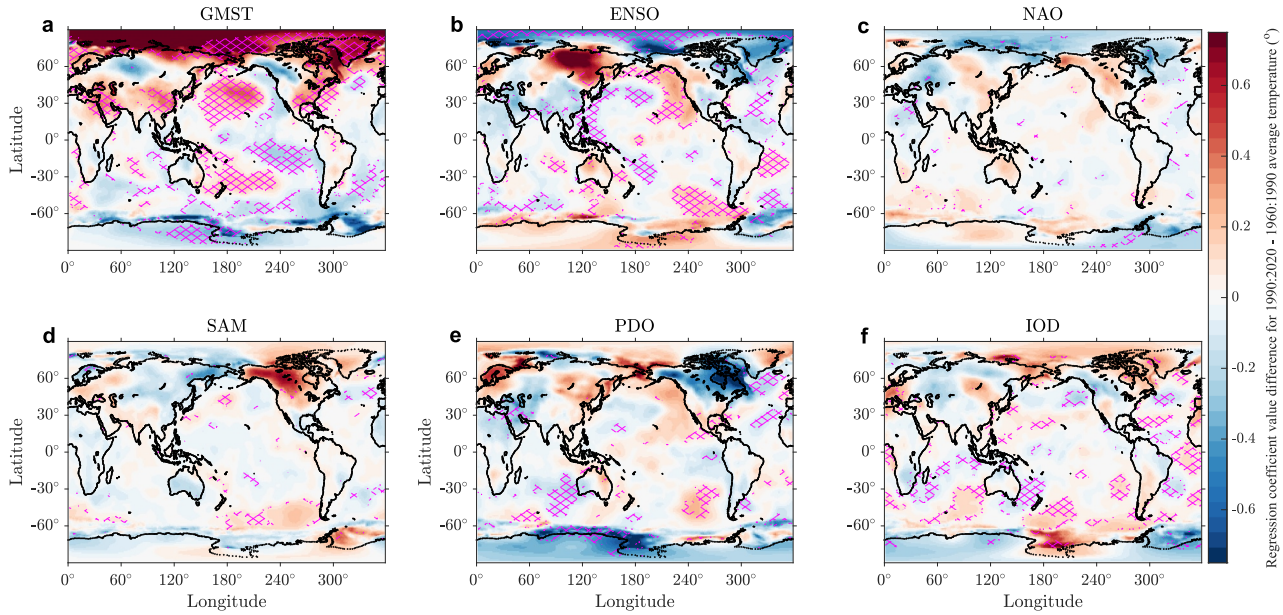

Figure 3. *Point-wise attribution*. Differences in regression coefficients between 1960–1990 and 1990–2020 for five internal variability modes and GMST. Positive values indicate increased co-variation of monthly temperatures with the corresponding mode. Locations where the differences between the periods can be attributed to anthropogenic climate change are indicated by pink crosses.

Returning to the two reasons that may lead to teleconnection changes, Table SI2 in Supporting Information S1 shows the variance of each index used in the regression analysis for each of the two periods. While the GMST variance has increased as expected due to the acceleration of warming in the latter period, the variance of other modes is basically unchanged. Note that the PDO time scale is decadal, and a 30-year period is insufficient to obtain a robust estimate of its variance. Based on these results, one may conclude that the teleconnection changes presented here and in the previous section arise not from changes in the modes themselves (e.g., ENSO), but from changes in the atmospheric medium through which these teleconnections propagate. This interpretation is supported by the fact that the time series of each mode (Figure SI10 in Supporting Information S1) shows no major shifts in behavior over the past 3 decades.

2.3. Projected Changes in Teleconnections

Finally, we examine how the teleconnections of these modes may further change in a warmer future climate by applying our multilinear regression analysis to the CESM2 large ensemble (Kay et al., 2015) under the RCP 8.5 scenario (Riahi et al., 2011). Maps of regression coefficient differences between 1960–1990 and 2070–2100 for the mean of the large ensemble are shown in Figure 4. Hatched regions represent locations where results are statistically insignificant (the 5–95 percentile range calculated over all ensemble members includes the zero value; note that this hatching represents a different meaning from that in Figure 3, hence the different hatching pattern and color used; see a complementary presentation of the same results in Figure SI15 in Supporting Information S1). The effects of GMST on monthly temperature increases, reflecting that a greater rate of warming is anticipated under RCP 8.5 in 2070–2100 relative to 1960–1990. We use the extreme RCP 8.5 scenario to maximize signal-to-noise ratio, but further examination of teleconnection changes for more modest—and perhaps more realistic—warming scenarios is warranted.

Projections of changes to ENSO teleconnections (Figure 4b) show amplification of some observed trends over the past decades, but the pattern of change is neither uniform nor simple. Positive teleconnections in Australia and Northern South America become stronger, as does a negative teleconnection in Southern South America (Figures SI11–SI13 in Supporting Information S1). The pattern over much of the Americas, however, generally weakens or changes. Other mode changes can be seen in the other panels of Figure 4. We also note that the effects of the

19448007, 2026, 2, Downloaded from https://agupubs.onlinelibrary.wiley.com/doi/10.1029/2025GL119307 by Weizmann Institute Of Science, Wiley Online Library on [15/01/2026]. See the Terms and Conditions (https://onlinelibrary.wiley.com/terms-and-conditions) on Wiley Online Library for rules of use; OA articles are governed by the applicable Creative Commons License

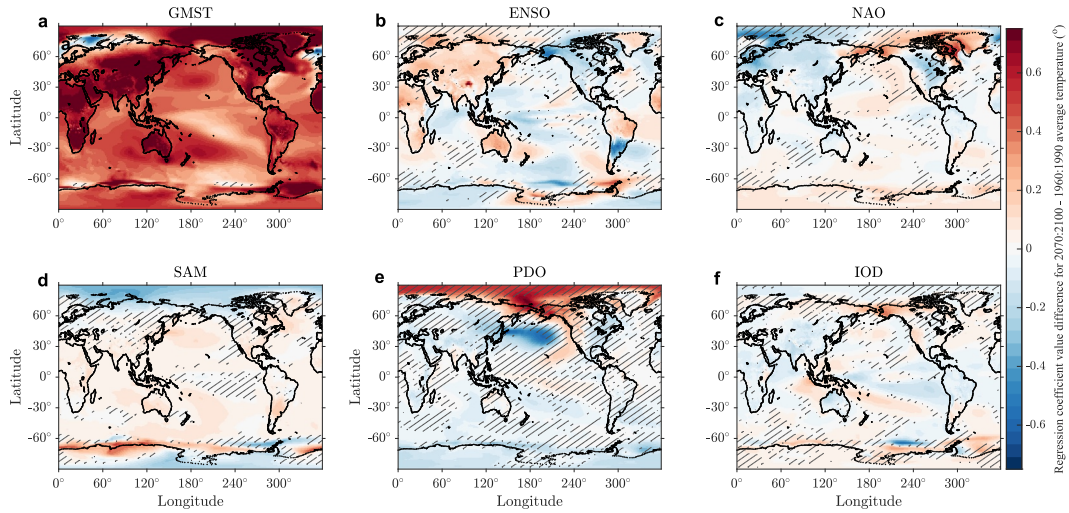

Figure 4. *Climate change projections*. Similar to Figure 3, but for the difference in regression coefficients between 1960–1990 and 2070–2100 using simulations. Temperatures and mode indices are from CESM2-LE simulations. In this case, locations where results are statistically insignificant are indicated by gray hatching.

NAO on monthly temperatures become less strong over Europe, hence, the difference is negative; that the PDO dipole structure in the North Pacific strengthens, and that the influence of the IOD dipole on monthly temperatures weakens locally as well as in South Asia and North Africa.

3. Summary and Discussion

We find statistically significant changes to teleconnection patterns of the major internal climate variability modes using two complementary attribution approaches. The monthly temperature-based covariance was found to change between 1960–1990 and 1990–2020 based on a covariance fingerprinting approach. To verify the robustness of these results, we applied two formulations: one that captures both the spatial pattern and amplitude of the covariance matrix (Figure 2), and an alternative formulation that evaluates the matrices in a manner more analogous to a correlation (Figure SI17 in Supporting Information S1). Both approaches yield consistent outcomes, capturing the historical changes in the covariance structure. Results are confirmed and extended to modes that are defined based on sea level pressure rather than temperature (NAO and SAM) using a point-wise attribution approach. This point-wise analysis suggests that ENSO teleconnections were altered by anthropogenic climate change in more than 20% of global grid cells. Similarly, IOD teleconnections have changed in over 15% of grid locations. Some teleconnections that pass the statistical significance test, such as the IOD effects on the Northern Hemisphere—would benefit from a more mechanistic understanding of the change to increase confidence in their patterns, although equivalent effects of the IOD were pointed out previously (Annamalai et al., 2007). Forced climate simulations that are found to capture historical changes (Figures 2 and 3) indicate that monthly temperature covariations will continue to change under a warming climate (Figure 4). This highlights that the effects of climate change on temperature go beyond global or regional averages and also alter the patterns of internal variation across most of the globe.

Conflict of Interest

The authors declare no conflicts of interest relevant to this study.

Data Availability Statement

The Niño 3.4 time series is available here: https://psl.noaa.gov/data/timeseries/monthly/Niño34.

The NAO and SAM time series are available here: https://psl.noaa.gov/data/20thC_Rean/timeseries.

The PDO time series is available here: https://psl.noaa.gov/pdo/.

19448007, 2026, 2, Downloaded from https://agupubs.onlinelibrary.wiley.com/doi/10.1029/2025GL119307 by Weizmann Institute Of Science, Wiley Online Library on [15/01/2026]. See the Terms and Conditions (https://onlinelibrary.wiley.com/terms-and-conditions) on Wiley Online Library for rules of use; OA articles are governed by the applicable Creative Commons License

The IOD time series is available here: https://psl.noaa.gov/data/timeseries/month/DMI/.

The SAM time series is available here: https://psl.noaa.gov/data/20thC_Rean/timeseries/monthly/SAM/.

The GMST time series is available here: https://www.ncei.noaa.gov/products/land-based-station/noaa-global-temp.

Post-processed data of CESM2-LE control run, historical run, and future RCP 8.5 run are available at https://www.earthsystemgrid.org/dataset/ucar.cgd.cesm2le.output.html.

Acknowledgments
ET was supported by the U.S. Department of Energy (DOE) Office of Science Biological and Environmental Research Grant DE-SC0023134, and thanks the Weizmann Institute of Science for its hospitality during parts of this work. EV was supported by the Council for Higher Education of Israel, under the project "Integrating Climate Dynamics, Clouds, and Extreme Events through Teleconnections in Climate Networks."

References

Alexander, M. A., Bladé, I., Newman, M., Lanzante, J. R., Lau, N.-C., & Scott, J. D. (2002). The atmospheric bridge: The influence of ENSO teleconnections on air–sea interaction over the global oceans. *Journal of Climate*, *15*(16), 2205–2231. https://doi.org/10.1175/1520-0442(2002)015<2205:tabtio>2.0.co;2

Anderson, W., Seager, R., Baethgen, W., & Cane, M. (2017). Life cycles of agriculturally relevant ENSO teleconnections in North and South America. *International Journal of Climatology*, *37*(8), 3297–3318. https://doi.org/10.1002/joc.4916

Annamalai, H., Okajima, H., & Watanabe, M. (2007). Possible impact of the Indian Ocean SST on the Northern Hemisphere circulation during El Niño. *Journal of Climate*, *20*(13), 3164–3189. https://doi.org/10.1175/jcli4156.1

Beverley, J., Collins, M., Lambert, F. H., & Chadwick, R. (2024). Drivers of changes to the ENSO–Europe teleconnection under future warming. *Geophysical Research Letters*, *51*(10), e2023GL107957. https://doi.org/10.1029/2023gl107957

Bilbao, R. A., Gregory, J. M., Bouttes, N., Palmer, M. D., & Stott, P. (2019). Attribution of ocean temperature change to anthropogenic and natural forcings using the temporal, vertical and geographical structure. *Climate Dynamics*, *53*(9), 5389–5413. https://doi.org/10.1007/s00382-019-04910-1

Burke, A., Sriver, R. L., & Long, M. S. (2017). A global perspective on the drivers of climate teleconnections. *Journal of Climate*, *30*(16), 6637–6659. https://doi.org/10.1175/JCLI-D-16-0244.1

Cai, W., McPhaden, M. J., Grimm, A. M., Rodrigues, R. R., Taschetto, A. S., Garreaud, R. D., et al. (2020). Climate impacts of the El Niño–Southern Oscillation on South America. *Nature Reviews Earth & Environment*, *1*(4), 215–231. https://doi.org/10.1038/s43017-020-0040-3

Cai, W., Ng, B., Geng, T., Jia, F., Wu, L., Wang, G., et al. (2023). Anthropogenic impacts on twentieth-century ENSO variability changes. *Nature Reviews Earth & Environment*, *4*(6), 407–418. https://doi.org/10.1038/s43017-023-00427-8

Cai, W., Van Rensch, P., Cowan, T., & Hendon, H. H. (2011). Teleconnection pathways of ENSO and the IOD and the mechanisms for impacts on Australian rainfall. *Journal of Climate*, *24*(15), 3910–3923. https://doi.org/10.1175/2011jcli4129.1

Casanueva, A., Rodríguez-Puebla, C., Frías, M., & González-Reviriego, N. (2014). Variability of extreme precipitation over Europe and its relationships with teleconnection patterns. *Hydrology and Earth System Sciences*, *18*(2), 709–725. https://doi.org/10.5194/hess-18-709-2014

Casselman, J. W., Lübbecke, J. F., Bayr, T., Huo, W., Wahl, S., & Domeisen, D. I. (2023). The teleconnection of extreme El Niño–Southern Oscillation (ENSO) events to the tropical North Atlantic in coupled climate models. *Weather and Climate Dynamics*, *4*(2), 471–487. https://doi.org/10.5194/wcd-4-471-2023

Danabasoglu, G., Lamarque, J.-F., Bacmeister, J., Bailey, D. A., DuVivier, A. K., Edwards, J., et al. (2020). The Community Earth System Model Version 2 (CESM2). *Journal of Advances in Modeling Earth Systems*, *12*(2), e2019MS001916. https://doi.org/10.1029/2019MS001916

Deser, C., Terray, L., & Phillips, A. S. (2017). Forced and internal components of winter air temperature trends over North America. *Nature Climate Change*, *7*, 552–556. https://doi.org/10.1038/nclimate3269

Galytska, E., Weigel, K., Handorf, D., Jaiser, R., Köhler, R., Runge, J., & Eyring, V. (2023). Evaluating causal Arctic-midlatitude teleconnections in CMIP6. *Journal of Geophysical Research: Atmospheres*, *128*(17), e2022JD037978. https://doi.org/10.1029/2022jd037978

Gershunov, A., & Barnett, T. P. (1998). Interdecadal modulation of ENSO teleconnections. *Bulletin of the American Meteorological Society*, *79*(12), 2715–2726. https://doi.org/10.1175/1520-0477(1998)079<2715:imoet>2.0.co;2

Gillett, N. P., Graf, H. F., & Osborn, T. J. (2003). Climate change and the North Atlantic oscillation. *Geophysical Monograph-American Geophysical Union*, *134*, 193–210.

Hamouda, M. E., Pasquero, C., & Tziperman, E. (2021). Decoupling of the Arctic Oscillation and North Atlantic Oscillation in a warmer climate. *Nature Climate Change*, *11*(2), 137–142. https://doi.org/10.1038/s41558-020-00966-8

Hardiman, S. C., Dunstone, N. J., Scaife, A. A., Smith, D. M., Knight, J. R., Davies, P., et al. (2020). Predictability of European winter 2019/20: Indian Ocean dipole impacts on the NAO. *Atmospheric Science Letters*, *21*(12), e1005. https://doi.org/10.1002/asl.1005

Hasselmann, K. (1979). *On the signal-to-noise problem in atmospheric response studies*. Royal Meteorological Society.

Hegerl, G. C., voN StoRcH, H., Hasselmann, K., Santer, B. D., Cubasch, U., & Jones, P. D. (1996). Detecting greenhouse-gas-induced climate change with an optimal fingerprint method. *Journal of Climate*, *9*(10), 2281–2306. https://doi.org/10.1175/1520-0442(1996)009<2281:dggicc>2.0.co;2

Hobeichi, S., Abramowitz, G., Sen Gupta, A., Taschetto, A. S., Richardson, D., Rampal, N., et al. (2024). How well do climate modes explain precipitation variability? *npj Climate and Atmospheric Science*, *7*(1), 1–9. https://doi.org/10.1038/s41612-024-00853-5

Hoerling, M. P., Hurrell, J. W., Xu, T., Bates, G. T., & Phillips, A. (2004). Twentieth century North Atlantic climate change. Part II: Understanding the effect of Indian Ocean warming. *Climate Dynamics*, *23*(3–4), 391–405. https://doi.org/10.1007/s00382-004-0433-x

Hoskins, B. J., & Karoly, D. J. (1981). The steady linear response of a spherical atmosphere to thermal and orographic forcing. *Journal of the Atmospheric Sciences*, *38*(6), 1179–1196. https://doi.org/10.1175/1520-0469(1981)038⟨1179:TSLROA⟩2.0.CO;2

Jones, G. S., Stott, P. A., & Mitchell, J. F. (2016). Uncertainties in the attribution of greenhouse gas warming and implications for climate prediction. *Journal of Geophysical Research: Atmospheres*, *121*(12), 6969–6992. https://doi.org/10.1002/2015jd024337

Joshi, M. K., Abid, M. A., & Kucharski, F. (2021). The role of an Indian Ocean heating dipole in the ENSO teleconnection to the North Atlantic European region in early winter during the twentieth century in reanalysis and CMIP5 simulations. *Journal of Climate*, *34*(3), 1047–1060. https://doi.org/10.1175/jcli-d-20-0269.1

Karoly, D. J. (1989). Southern hemisphere circulation features associated with El Niño-Southern Oscillation events. *Journal of Climate*, *2*(11), 1239–1252. https://doi.org/10.1175/1520-0442(1989)002<1239:shcfaw>2.0.co;2

19448007, 2026, 2, Downloaded from https://agupubs.onlinelibrary.wiley.com/doi/10.1029/2025GL119307 by Weizmann Institute Of Science, Wiley Online Library on [15/01/2026]. See the Terms and Conditions (https://onlinelibrary.wiley.com/terms-and-conditions) on Wiley Online Library for rules of use; OA articles are governed by the applicable Creative Commons License

Kay, J. E., Deser, C., Phillips, A., Mai, A., Hannay, C., Strand, G., et al. (2015). The Community Earth System Model (CESM) large ensemble project: A community resource for studying climate change in the presence of internal climate variability. *Bulletin of the American Meteorological Society*, *96*(8), 1333–1349. https://doi.org/10.1175/bams-d-13-00255.1

King, M. P., Kucharski, F., & Molteni, F. (2010). The roles of external forcings and internal variabilities in the Northern Hemisphere atmospheric circulation change from the 1960s to the 1990s. *Journal of Climate*, *23*(23), 6200–6220. https://doi.org/10.1175/2010jcli3239.1

Kosaka, Y., & Xie, S.-P. (2013). Recent global-warming hiatus tied to equatorial Pacific surface cooling. *Nature*, *501*(7467), 403–407.

Kumar, K. N., Molini, A., Ouarda, T. B., & Rajeevan, M. N. (2017). North Atlantic controls on wintertime warm extremes and aridification trends in the Middle East. *Scientific Reports*, *7*(1), 12301. https://doi.org/10.1038/s41598-017-12430-3

Kurths, J., Agarwal, A., Shukla, R., Marwan, N., Rathinasamy, M., Caesar, L., et al. (2019). Unravelling the spatial diversity of Indian precipitation teleconnections via a non-linear multi-scale approach. *Nonlinear Processes in Geophysics*, *26*(3), 251–266. https://doi.org/10.5194/npg-26-251-2019

Lieber, R., Brown, J., King, A., & Freund, M. (2024). Historical and future asymmetry of ENSO teleconnections with extremes. *Journal of Climate*, *37*(22), 5909–5924. https://doi.org/10.1175/jcli-d-23-0619.1

Linderholm, H. W., Ou, T., Jeong, J.-H., Folland, C. K., Gong, D., Liu, H., et al. (2011). Interannual teleconnections between the summer North Atlantic Oscillation and the East Asian summer monsoon. *Journal of Geophysical Research*, *116*(D13), D13107. https://doi.org/10.1029/2010jd015235

Paeth, H., & Pollinger, F. (2010). Enhanced evidence in climate models for changes in extratropical atmospheric circulation. *Tellus A: Dynamic Meteorology and Oceanography*, *62*(5), 647–660. https://doi.org/10.1111/j.1600-0870.2010.00455.x

Power, S. B., Delage, F. P., Chung, C., Kociuba, G., & Keay, K. (2013). Robust twenty-first-century projections of El Niño and related precipitation variability. *Nature*, *502*(7472), 541–545. https://doi.org/10.1038/nature12580

Reboita, M. S., Ambrizzi, T., Crespo, N. M., Dutra, L. M. M., Ferreira, G. W. D. S., Rehbein, A., et al. (2021). Impacts of teleconnection patterns on South America climate. *Annals of the New York Academy of Sciences*, *1504*(1), 116–153. https://doi.org/10.1111/nyas.14592

Riahi, K., Rao, S., Krey, V., Cho, C., Chirkov, V., Fischer, G., et al. (2011). RCP 8.5—A scenario of comparatively high greenhouse gas emissions. *Climatic Change*, *109*(1–2), 33–57. https://doi.org/10.1007/s10584-011-0149-y

Ribes, A., Azaïs, J.-M., & Planton, S. (2009). Adaptation of the optimal fingerprint method for climate change detection using a well-conditioned covariance matrix estimate. *Climate Dynamics*, *33*(5), 707–722. https://doi.org/10.1007/s00382-009-0561-4

Rohde, R. A., & Hausfather, Z. (2020). The Berkeley Earth land/ocean temperature record. *Earth System Science Data Discussions*, *2020*(4), 1–16. https://doi.org/10.5194/essd-12-3469-2020

Roy, I., Tedeschi, R., & Collins, M. (2016). ENSO teleconnections to the Indian summer monsoon in observations and models. *International Journal of Climatology*, *37*(4), 1794–1813. https://doi.org/10.1002/joc.4811

Saji, N., Ambrizzi, T., & Ferraz, S. E. T. (2005). Indian Ocean dipole mode events and austral surface air temperature anomalies. *Dynamics of Atmospheres and Oceans*, *39*(1–2), 87–101. https://doi.org/10.1016/j.dynatmoce.2004.10.015

Sandler, D., Saaroni, H., Ziv, B., Tamarin-Brodsky, T., & Harnik, N. (2024). The connection between North Atlantic storm track regimes and eastern Mediterranean cyclonic activity. *Weather and Climate Dynamics*, *5*(3), 1103–1116. https://doi.org/10.5194/wcd-5-1103-2024

Shi, N., Tian, P., & Zhang, L. (2019). Simultaneous influence of the Southern Hemisphere annular mode on the atmospheric circulation of the Northern Hemisphere during the boreal winter. *International Journal of Climatology*, *39*(5), 2685–2696. https://doi.org/10.1002/joc.5981

Simon Wang, S.-Y., Huang, W.-R., Hsu, H.-H., & Gillies, R. R. (2015). Role of the strengthened El Niño teleconnection in the May 2015 floods over the southern Great Plains. *Geophysical Research Letters*, *42*(19), 8140–8146. https://doi.org/10.1002/2015gl065211

Wallace, J. M., & Gutzler, D. S. (1981). Teleconnections in the geopotential height field during the Northern Hemisphere winter. *Monthly Weather Review*, *109*(4), 784–812. https://doi.org/10.1175/1520-0493(1981)109<0784:titghf>2.0.co;2

Wang, G., & Schimel, D. (2003). Climate change, climate modes, and climate impacts. *Annual Review of Environment and Resources*, *28*(1), 1–28. https://doi.org/10.1146/annurev.energy.28.050302.105444

Xie, S.-P., Deser, C., Vecchi, G. A., Ma, J., Teng, H., & Wittenberg, A. T. (2010). Global warming pattern formation: Sea surface temperature and rainfall. *Nature Geoscience*, *3*, 151–160. https://doi.org/10.1038/ngeo749

Yang, X., & DelSole, T. (2012). Systematic comparison of ENSO teleconnection patterns between models and observations. *Journal of Climate*, *25*(2), 425–446. https://doi.org/10.1175/jcli-d-11-00175.1

Yeh, S.-W., Cai, W., Min, S.-K., McPhaden, M. J., Dommenget, D., Dewitte, B., et al. (2018). ENSO atmospheric teleconnections and their response to greenhouse gas forcing. *Reviews of Geophysics*, *56*(1), 185–206. https://doi.org/10.1002/2017rg000568

Zebiak, S. E., Orlove, B., Muñoz, Á. G., Vaughan, C., Hansen, J., Troy, T., et al. (2015). Investigating El Niño-Southern Oscillation and society relationships. *Wiley Interdisciplinary Reviews: Climate Change*, *6*(1), 17–34. https://doi.org/10.1002/wcc.294

Zhou, L., Hua, W., Nicholson, S. E., & Clark, J. P. (2024). Interannual teleconnections in the Sahara temperatures associated with the North Atlantic Oscillation (NAO) during boreal winter. *Climate Dynamics*, *62*(2), 1123–1143. https://doi.org/10.1007/s00382-023-06962-w

References From the Supporting Information

Hou, Y., Xie, S.-P., Johnson, N. C., Wang, C., Yoo, C., Deng, K., et al. (2024). Unveiling the Indian Ocean forcing on winter eastern warming–western cooling pattern over North America. *Nature Communications*, *15*(1), 9654. https://doi.org/10.1038/s41467-024-53921-y

Hurrell, J. W. (1995). Decadal trends in the north Atlantic oscillation: Regional temperatures and precipitation. *Science*, *269*(5224), 676–679. https://doi.org/10.1126/science.269.5224.676

Mantua, N. J., Hare, S. R., Zhang, Y., Wallace, J. M., & Francis, R. C. (1997). A Pacific interdecadal climate oscillation with impacts on salmon production. *Bulletin of the American Meteorological Society*, *78*(6), 1069–1080. https://doi.org/10.1175/1520-0477(1997)078<1069:apicow>2.0.co;2

Marshall, G. J. (2003). Trends in the southern annular mode from observations and reanalyses. *Journal of Climate*, *16*(24), 4134–4143. https://doi.org/10.1175/1520-0442(2003)016<4134:titsam>2.0.co;2

Montgomery, D. C., Peck, E. A., & Vining, G. G. (2021). *Introduction to linear regression analysis*. John Wiley & Sons.

North, G. R., Bell, T. L., Cahalan, R. F., & Moeng, F. J. (1982). Sampling errors in the estimation of empirical orthogonal functions. *Monthly Weather Review*, *110*(7), 699–706. https://doi.org/10.1175/1520-0493(1982)110<0699:seiteo>2.0.co;2

Saji, N., Goswami, B. N., Vinayachandran, P., & Yamagata, T. (1999). A dipole mode in the tropical Indian Ocean. *Nature*, *401*(6751), 360–363. https://doi.org/10.1038/43854

19448007, 2026, 2, Downloaded from https://agupubs.onlinelibrary.wiley.com/doi/10.1029/2025GL119307 by Weizmann Institute Of Science, Wiley Online Library on [15/01/2026]. See the Terms and Conditions (https://onlinelibrary.wiley.com/terms-and-conditions) on Wiley Online Library for rules of use; OA articles are governed by the applicable Creative Commons License

Climate change alters teleconnections Supporting Information

E. Vos[1], P. Huybers[2], E.Tziperman[2]

[1]Laboratoire de Météorologie Dynamique/IPSL, Sorbonne Université, ENS,PSL Research University, Ecole Polytechnique, CNRS, Paris France.
[2]Department of Earth and Planetary Sciences and School of Engineering and Applied Sciences, Harvard University, Cambridge, MA, USA.

Contents of this file

Supporting Information results text
Methods
Figure SI1-18
Tables S1-S2

Corresponding author: Eran Vos, eran.vos@gmail.com

Data and Methods

Data

All the data we use is publicly available in the following locations: The Niño 3.4 time series is available here: https://psl.noaa.gov/data/timeseries/monthly/Niño34. The NAO and SAM time series are available here: https://psl.noaa.gov/data/20thC_Rean/timeseries. The PDO time series is available here: https://psl.noaa.gov/pdo/ The IOD time series is available here: https://psl.noaa.gov/data/timeseries/month/DMI/ The SAM time series is available here: https://psl.noaa.gov/data/20thC_Rean/timeseries/monthly/SAM/ The GMST time series is available here: https://www.ncei.noaa.gov/products/land-based-station/noaa-global-temp Post-processed data of CESM2-LE control run, historical run, and future RCP 8.5 run are available at https://www.earthsystemgrid.org/dataset/ucar.cgd.cesm2le.output.html For the forced and future model runs, we use the entire model ensemble.

Covariance fingerprinting

Consider data vectors $\mathbf{z}_i$ of monthly SST anomaly at all grid points arranged in the matrix Z:

$$Z = (\mathbf{z}_1, \cdots, \mathbf{z}_N),$$

and the covariance matrix C,

$$C = ZZ^T/(N-1).$$

We consider several specific covariance matrices. First, from greenhouse forced simulations for the two periods, 1960–1990, 1990–2020: $C^{\text{model}}_{\text{forced},1990}(j)$ and $C^{\text{model}}_{\text{forced},2020}(j)$. The index j corresponds to the ensemble member in the large ensemble of such forced runs; here, we use the full ensemble of 100 members. Similarly, for observations for these two periods, C^{obs}_{1990} and C^{obs}_{2020}. Finally, taking two consecutive 30-year periods from a long control run, denoting each pair of such periods with an index i, we have two such matrices $C^{\text{model}}_{\text{ctr}}(i,1)$ and $C^{\text{model}}_{\text{ctr}}(i,2)$. We wish to test if the difference between the two observed covariance matrices is due to climate change.

To answer the above question, we define the differences between covariance matrices,

$$\begin{aligned}
\Delta C^{\text{model}}_{\text{ctr}}(i) &= C^{\text{model}}_{\text{ctr}}(i,2) - C^{\text{model}}_{\text{ctr}}(i,1) \\
\Delta C^{\text{model}}_{\text{forced}} &= \text{mean}(C^{\text{model}}_{\text{forced},2020}(j) - C^{\text{model}}_{\text{forced},1990}(j)) \\
\Delta C^{\text{obs}} &= C^{\text{obs}}_{2020} - C^{\text{obs}}_{1990}.
\end{aligned}$$

Next, we define a fingerprinting measure that quantifies the similarity of the model and observational change in covariance,

$$S^{\text{obs}} = \frac{\langle \Delta C^{\text{obs}}, \Delta C^{\text{model}}_{\text{forced}} \rangle_F}{\| \Delta C^{\text{model}}_{\text{forced}} \|^2_F}. \tag{1}$$

Note that we are interested in both the pattern of ΔC and in its amplitude. For example, if the observed change in covariance has exactly the same pattern as predicted by the models but is twice as large as, we want S to reflect this. This can be compared to a distribution based on the control run,

$$S^{\text{null}}_i = \frac{\langle \Delta C^{\text{model}}_{\text{ctr}}(i), \Delta C^{\text{model}}_{\text{forced}} \rangle_F}{\| \Delta C^{\text{model}}_{\text{forced}} \|^2_F}.$$

Where we have used Frobenius inner product: $\langle A, B\rangle = \sum_{ij} A_{ij}B_{ij} = \mathrm{tr}(A^T B)$, and the Frobenius norm (squared) is: $\|A\|_F^2 = \sum_{ij} A_{ij}^2$. Then we compare the value of the S^{obs} to the distribution of S^{null}

To ensure the robustness of our results, we also tested an alternative formulation that evaluates the matrices in a manner more analogous to a correlation—emphasizing the spatial pattern of covariance changes while remaining insensitive to their amplitude.

$$S^{\mathrm{obs}}_{\mathrm{alternative}} = \frac{\left\langle \Delta C^{\mathrm{obs}}, \Delta C^{\mathrm{model}}_{\mathrm{forced}} \right\rangle_F}{\|\Delta C^{\mathrm{obs}}\|_F \cdot \|\Delta C^{\mathrm{model}}_{\mathrm{forced}}\|_F}. \tag{2}$$

The results for the alternative approach are shown in Fig. SI17.

Contour plots of the weighted covariance. Define a weight w_i for each grid point in a relevant domain, say Niño3.4. The index i goes over all grid points (all latitudes and longitudes). We average the rows of the covariance matrix corresponding to each mode of variability using,

$$\overline{C}_j = \frac{\sum_i w_i C_{ij}}{\sum_i w_i} \tag{3}$$

For the GMST, we choose the weights to be w_i, the cosine of the corresponding latitude. For Niño3.4, we choose the weight to be 1 over the equatorial Niño3.4 region, and zero elsewhere. For the PDO, we select the rectangle between the southwest corner (20N, 130E) and the northeast corner (62N, 260E). We then set the weight w_i to the temperature signal corresponding to the PDO, as seen in Figure SI1 (panel e), within the specified rectangle, multiplied by the cosine of the corresponding latitude. Grid points that are not significant in that figure are masked and are not used for the averaging. A similar procedure is followed for the IOD, using the southwest corner (10S, 50E) and the northeast corner (10N, 108E).

Regional covariance fingerprinting. We also calculate the S measure on a regional basis, to test the significance of changes to the covariance structure of individual internal variability modes such as ENSO. For that purpose, we can define, for example,

$$S^{\mathrm{obs}}_{ENSO} = \frac{\left\langle \Delta C^{\mathrm{obs}}, \Delta C^{\mathrm{model}}_{\mathrm{forced}} \right\rangle_F^{ENSO}}{\left(\|\Delta C^{\mathrm{model}}_{\mathrm{forced}}\|_F^{ENSO}\right)^2},$$

where the ENSO superscripts indicate that we are summing the Frobenius norm and product only over the Niño3.4 region,

$$\langle A, B\rangle_F^{ENSO} = \sum_i \sum_j M_i^{ENSO} A_{ij} B_{ij},$$
$$\left(\|A\|_F^{ENSO}\right)^2 = \sum_i \sum_j M_i^{ENSO} A_{ij}^2,$$
$$M_i^{ENSO} = \begin{cases} 1 & \text{if } i \in \text{Nino3.4} \\ 0 & \text{elsewhere} \end{cases}$$

In the expression for the inner product, for example, we are summing only over rows of the covariance matrix in the Niño3.4 region (given the mask which is nonzero only for $i \in$ Niño3.4) with global monthly temperatures (all values of j). For the IOD we use 50°E–70°E, 10°S–10°N and 90°E–110°E, 10°S–0°.

In other words, it represents the covariance-weighted relationship between the index region and each grid point of the global temperature field T.

Comparison of covariance fingerprinting and multiple linear regression. This test evaluates the pattern correlation between the covariance fingerprinting and MLR results. In this context, X corresponds to the covariance fingerprinting results, Y to the MLR results, and i, j represent longitude and latitude, respectively. Given two fields as a function of latitude and longitude, X_{ij} and Y_{ij}, we examine their pattern correlation:

$$C_{XY} = \frac{\sum_{ij} X'_{ij} Y'_{ij}}{\left(\sum_{ij} X'^2_{ij}\right)^{1/2} \left(\sum_{ij} Y'^2_{ij}\right)^{1/2}}$$

where primed quantities indicate those after removing the mean. The pattern correlation between the covariance fingerprinting patterns obtained by averaging over the appropriate grid points and the multi linear regression results. The pattern correlation analysis are: C_{GMST}=0.7746, C_{ENSO}=0.9764, and C_{IOD}=0.5888. These relatively high values indicate that the two analysis approaches are closely related, but not identical.

Multi linear regression. To compute the contribution of each internal variability mode, we employ multilinear regression, which uses several explanatory variables to predict the outcome of a response variable. For example, we use the GMST and the mode time series to explain the average temperature anomaly.

$$\begin{aligned} T_{avg}(t,x) = a + c_1(x)\overline{T}(t) + c_2(x)Nino3.4(t) + c_3(x)NAO(t) \\ + c_4(x)SAM(t) + c_5(x)PDO(t) + c_6(x)IOD(t) \end{aligned} \tag{4}$$

Coefficients are obtained that minimize the LHS minus the RHS squared over the years of our analysis. The indices on the RHS are standardized (mean removed, divided by std) and orthogonalized using the Gram-Schmidt method. The orthogonalization turns the geometry of multiple regression into "independent axes," which simplifies interpretation, inference, and computation without changing the fitted values (Montgomery et al., 2021). The approach that we take is to evaluate orthogonalized versions of the indices. We begin with the GMST without any changes, and then remove GMST covariation from the ENSO index. We similarly proceed by removing covariation with foregoing modes for the NAO, SAM, PDO, and IOD. We address GMST and ENSO first, as these modes account for the greatest amount of temperature variability, though note that the listing of others is somewhat arbitrary. When orthogonalization is omitted, the results change only slightly, consistent with the weak inter-mode correlations (Figure SI16). An alternative approach is to apply SVD to the data matrix composed of 6 modes (GMST, ENSO, NAO, SAM, PDO, and IOD) and 60 years of monthly data. We find that the singular values for the period beginning in 1960 are 25.3, 20.1, 19.3, 19.0, 15.6, 11.7. Singular values for the period beginning in 199 are 22.3, 21.4, 19.4, 18.8, 16.9, 13.6. The North test (North et al., 1982) indicates that, for the 1960–1990 period, mode 1 is distinct, modes 2–4 form a degenerate group, and modes 5 and 6 are distinct. For the 1990–2020 period, SVD shows that modes 1–2 form a degenerate pair, modes 3–4 form a second degenerate pair, and modes 5 and 6 remain distinct. Given the presence of degenerate modes in both periods, orthogonalization is required to ensure a consistent basis for comparing the spatial patterns across time. We prefer the sequential removal of covariation in order to allow for physically-meaningful interpretation of actual climatic changes, as opposed to rotations within degenerate subspaces. This method has been used to calculate the contribution of the modes to the average temperature anomaly. When applying the Gram–Schmidt orthogonalization, part of the shared variance among indices is removed. For instance, the correlation between ENSO and PDO (0.469) is eliminated.

To test if the results are significant, we randomize the response variable 1000 times (bootstrapping) and calculate the regression coefficients; then, we compare the results to the 5th and 95th percentiles. In this case, we subtract the coefficients between the two periods. We randomize the response variable 1000 times for each period, calculate the contribution coefficients, and then subtract the coefficients between the periods. We also

tested the effect of randomizing the response variable in the phase diagram. The randomized test produced results similar to the main analysis (compare Fig. SI1 with Fig. SI18).

The teleconnections of the GMST and the five internal variability modes

Before examining the effects of climate change, we examine the contribution of each Internal Variability Mode to the monthly average global temperature anomalies by calculating the MLR between the monthly indices of the GMST, ENSO, NAO, SAM, PDO, and IOD to the monthly average temperature between the years 1950–2020. The six panels in Fig. SI1 show the regression coefficients that multiply each internal mode standardized index (see Method section). Positive values indicate co-variation of the monthly temperature at this location and the corresponding index. The hatching represents locations where the correlation is not statistically significant (see Methods section). The regression coefficient corresponding to the GMST is positive almost everywhere, with the Arctic warming amplification evident.

In addition to the obvious positive correlation in the equatorial Pacific Ocean, ENSO's coefficient is positive over Australia, South America, South Africa, India, and Western North America, indicating a warming trend during El Niño events or cooling during La Niña events. The negative signature over Greenland, Southern North America, the Arctic, and locations in mid-northern Asia indicates an anti-correlation between the monthly temperature there and the ENSO index.

The regression coefficient corresponding to the GMST is positive almost everywhere, with the Arctic warming amplification evident. In addition to the obvious positive correlation in the equatorial Pacific Ocean, ENSO's coefficient is positive over Australia, South America, South Africa, India, Australia, and Western Northern America, indicating a warming there during El-Niño events or cooling during La Niña events. The negative signature over Greenland, Southern North America, the Arctic, and locations in mid-northern Asia indicates an anti-correlation between the monthly temperature there and the ENSO index. Some of these ENSO teleconnections are well-established, such as the positive correlation of the NINO3.4 index and the surface temperature over Australia (Cai et al., 2011; Yang & DelSole, 2012), and similarly, correlations with South America (Cai et al., 2020; Anderson et al., 2017; Yang & DelSole, 2012), South Africa (Yang & DelSole, 2012), India (Yang & DelSole, 2012; Roy et al., 2016), North Asia (Yang & DelSole, 2012), and southern North America (Yang & DelSole, 2012). The other IVMs show the known regional results, such as NAO dipole between Greenland and Northwestern Europe (Hurrell, 1995), SAM anti-correlation to Antarctica (Thompson & Wallace, 2000; Marshall, 2003), PDO correlation with Northwestern North America (Mantua et al., 1997), and the IOD anti-correlation with Australia (Saji et al., 1999). In addition, there are also interesting remote correlations, such as NAO anti-correlation with the Sahara Desert in Africa (Zhou et al., 2024) and the Middle East (Kumar et al., 2017; Sandler et al., 2024), positive correlation with East Asia (Linderholm et al., 2011), SAM positive correlation with locations in the Northern Hemisphere(Shi et al., 2019), PDO correlation with northern Australia and some locations in Africa, and the IOD positive correlation with southern South America (Saji et al., 2005). Some modes exhibit stronger or weaker teleconnections when examined seasonally. For example, the NAO has a more pronounced influence over Europe during DJF (Hurrell, 1995), and positive IOD events have been linked to colder temperatures over North America in winter (Hou et al., 2024).

Climate change attribution process for the periods 2020:1990–1960:1990

We next examine whether these statistically significant changes between 1960–1990 and 1990–2020 are better explained by natural variability or anthropogenic climate change. For this, we use the Community Earth System Model Version 2 Large Ensemble runs

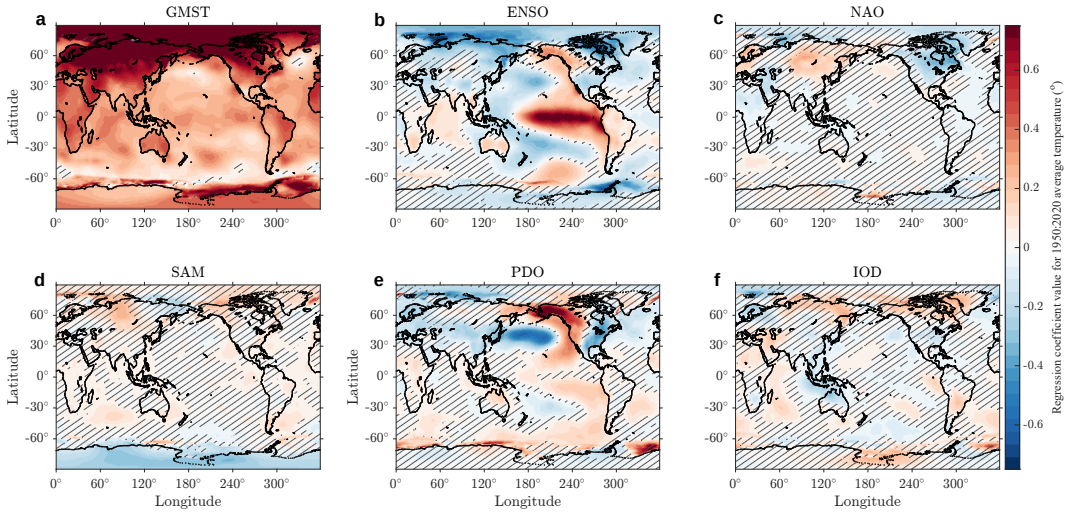

Figure SI1. Regression coefficients between standardized time series for several internal climate variability modes and the local monthly average temperature, calculated for 1950–2020. Positive values indicate co-variation of the monthly temperature at this location and the corresponding mode. Hatching represents locations where the results are not statistically significant. Not surprisingly, the regression coefficient corresponding to GMST (panel a) is positive almost everywhere, with evident Arctic warming amplification. The ENSO regression coefficient (panel b) shows the expected covariability over the equatorial Pacific and some other teleconnections.

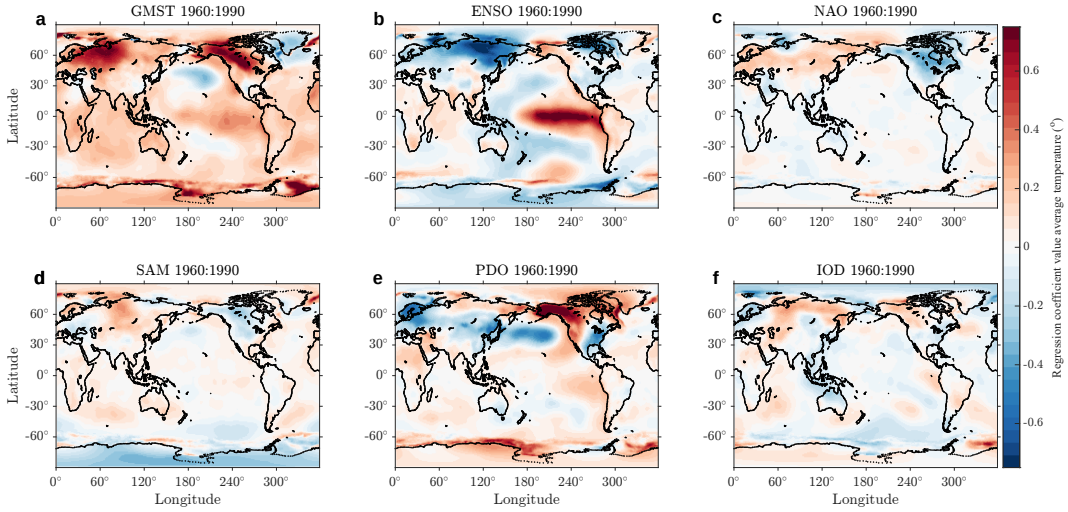

Figure SI2. Regression coefficients between standardized and orthogonalized time series for several internal climate variability modes and the local monthly average temperature, calculated for 1960-1990 from observations.

(CESM2-LE) (Danabasoglu et al., 2020; Kay et al., 2015). We compare the change in regression coefficients between the two periods, based on observations from both the control run that excludes a change in radiative forcing and the historical runs, where anthropogenic greenhouse forcing is applied. CESM2 simulates modes with some degree of realism (Figs. SI10,11). The teleconnection patterns during 1950–2020 are also sim-

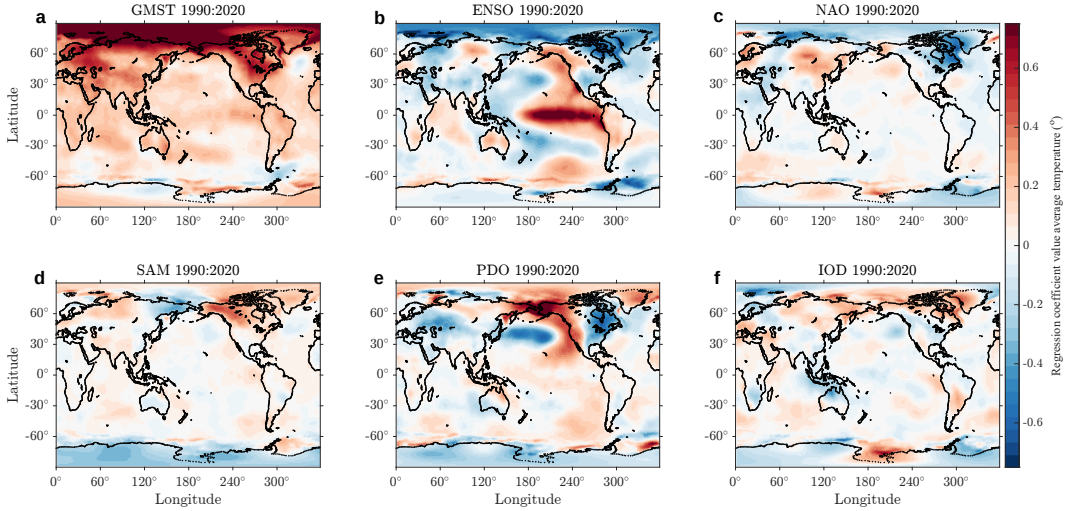

Figure SI3. Regression coefficients between standardized and orthogonalized time series for several internal climate variability modes and the local monthly average temperature, calculated for 1990-2020 from observations.

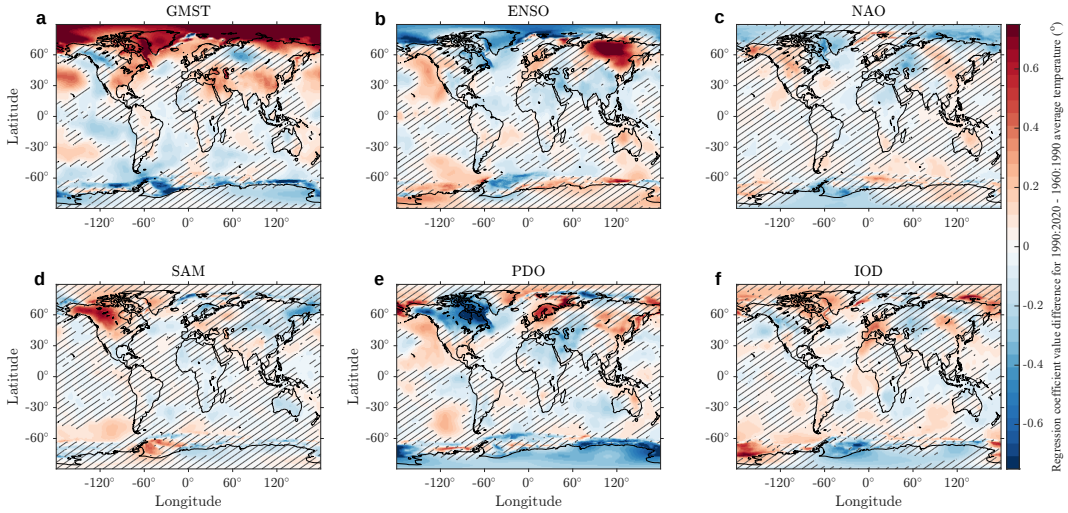

Figure SI4. Changes in internal variability patterns. Regression coefficients between standardized and orthogonalized time series for the GMST, the five internal variability modes, and the local monthly average temperature. Shown are the differences in the regression coefficients between the periods 2020–1990 (Fig. SI3) and 1960–1990 (Fig. SI2). Hatched locations indicate the results that are not statistically significant.

ulated relatively well (compare Figs. SI5 and SI1), although the magnitude of the corresponding regression coefficients (Fig. SI9) doesn't always match the observed (Fig. SI10).

As the first step in this attribution calculation, we examine if the forced model runs can reproduce the observed difference in the regression coefficients between 1960–1990 and 1990–2020 (Fig. SI6). If they do, it would provide evidence that further model analysis discussed below can be used to attribute the observed change to anthropogenic climate change. The colors show the differences in regression coefficients between the two periods, as in the corresponding Fig. SI4 for the observations. Unhatched areas are lo-

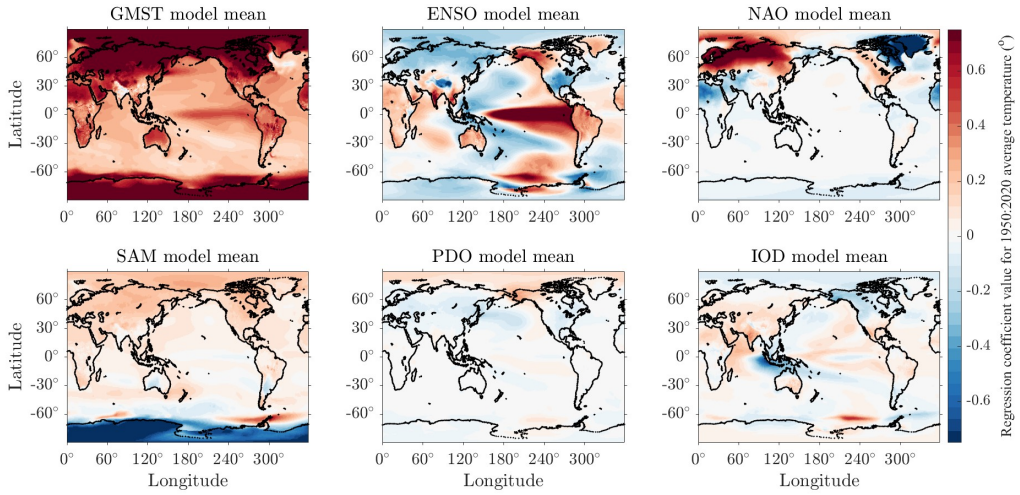

Figure SI5. CESM2-LE regression coefficients mean between standardized and orthogonalized time series for several internal climate variability modes and the local monthly average temperature, calculated for 1950-2020.

cations where at least 2.5% of the forced model historical ensemble members found a change in regression coefficient that is larger than the positive observed changes or smaller than the negative observed changes. Hatched areas are therefore those where the model's forced trend plus natural variability are inconsistent with the observed signal, and therefore these are the areas where the models cannot be trusted for climate change attribution purposes. Note that most areas are not hatched, indicating that the forced ensemble members are largely capable of reproducing the observed signal. Two noticeable hatched locations are the GMST West Arctic and ENSO big differences in North East Asia.

Next, we address the attribution of an anthropogenic climate change signal by comparing the observed change in regression coefficients between the two periods with those of the unforced control run ensemble members. To test whether natural variability alone can explain the observed change in the regression coefficients seen in Fig. SI4, we compare the observed changes between the two periods to differences between randomly selected pairs of 30-year windows from the pre-industrial control run (Fig. SI7). The color shading represents the change in the observed regression coefficients, as in Fig. SI4. We test whether the observed regression change between the two periods may be a result of random internal variability. For this purpose, we calculate the distribution of such changes from the long control run and require that the observed change be in the lowest 2.5% or highest 2.5% of the distribution for it not to be explained by natural variability. The hatched areas are locations where the observed differences in the regression coefficients seen in Fig. SI4 are judged not to be in the highest or lowest percentiles and are therefore consistent with natural variability.

Regional covariance fingerprinting

We explore the contribution of regional covariance fingerprinting (See Methods), an expansion from a specific region to the rest of the grid points to S_{obs} . Fig. SI14 shows an expansion of the covariance fingerprinting from the Niño 3.4, and the Indian Ocean regions to all grid points. We find strong similarities for GMST (all grid points) and for the IOD ($S = 0.107$). In contrast, ENSO shows a more mixed pattern: some regions, such as North Asia, exhibit notable agreement, while others do not. This discrepancy may

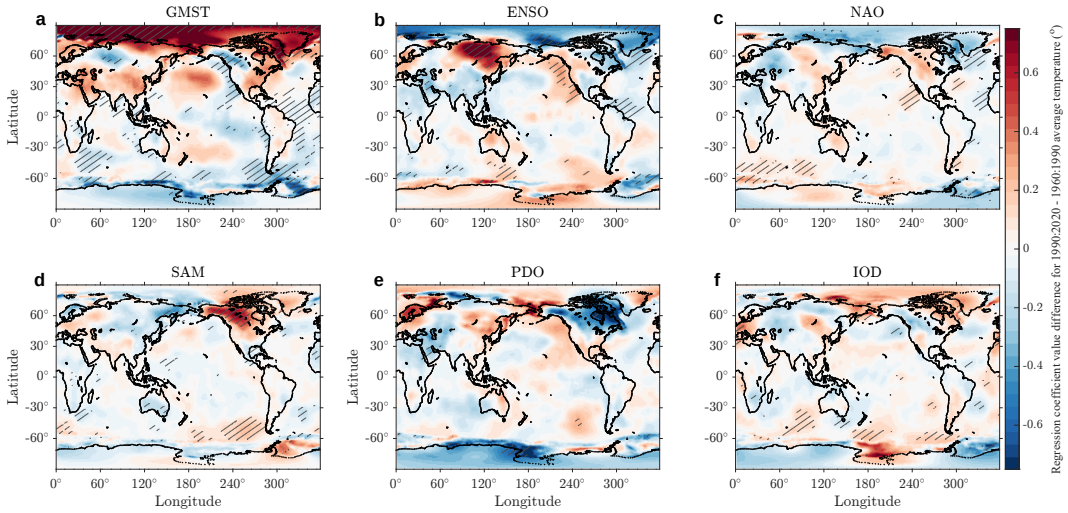

Figure SI6. Regression coefficients between standardized and orthogonalized time series for the GMST and the five internal variability modes and the local monthly average temperature. Shown are the differences in the regression coefficients between the periods 2020–1990 (Fig. SI3) and 1960–1990 (Fig. SI2) from Fig.SI4. Hatched areas are locations where CESM2-LE historical run with a changing forcing cannot reproduce the observations.

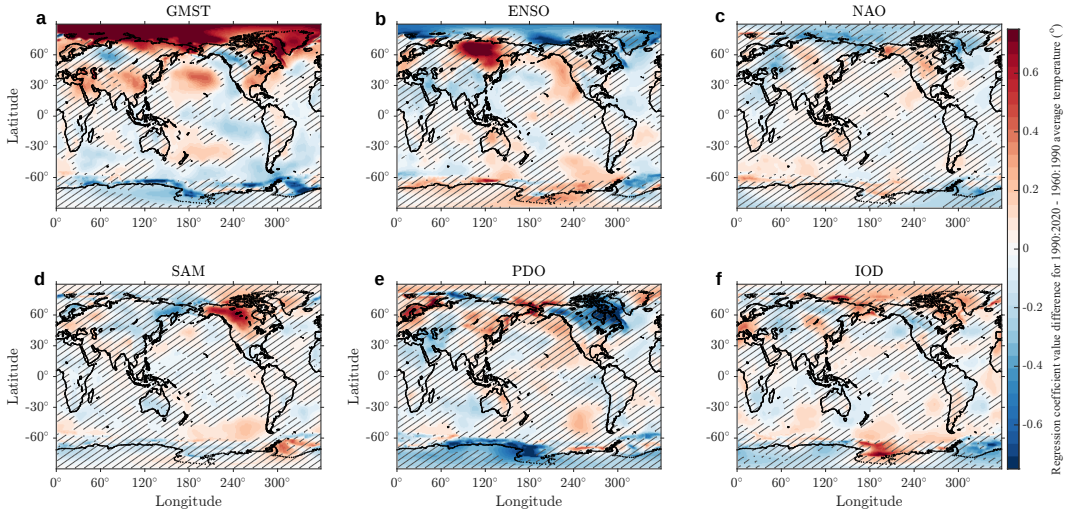

Figure SI7. Regression coefficients between standardized and orthogonalized time series for the GMST and the five internal variability modes and the local monthly average temperature. Shown are the differences in the regression coefficients between the periods 2020–1990 (Fig. SI3) and 1960–1990 (Fig. SI2) from Fig.SI4. Hatched areas are locations where CESM2-LE pre-industrial control run with a constant forcing can reproduce the observations.

stem from the fact that El Niño and La Niña produce distinct teleconnection patterns, and the forced model simulations may represent different relative frequencies of each phase.

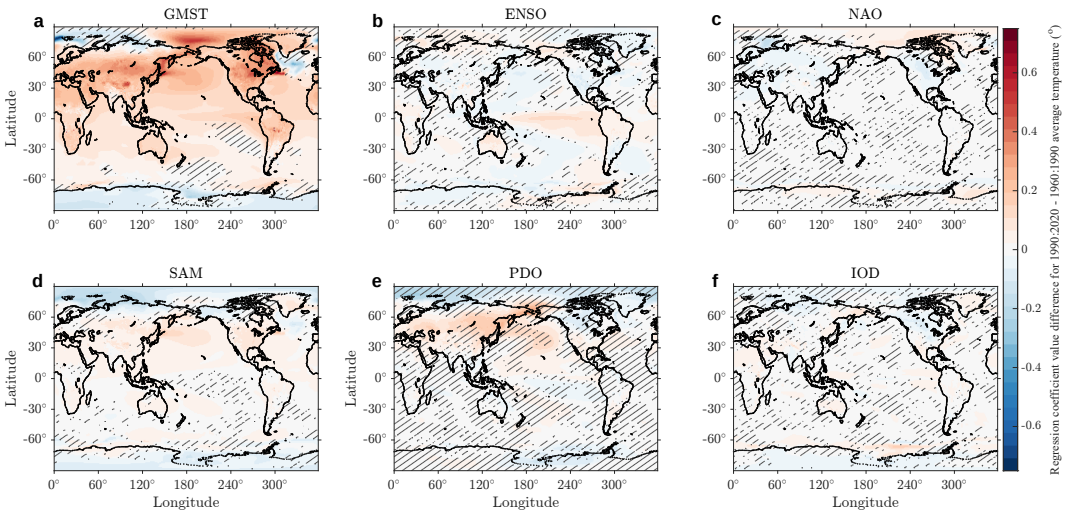

Figure SI8. CESM2-LE mean difference in the regression coefficients between 1990-2020 and 1960-1990. Hatching represents locations where the results are not statistically significant.

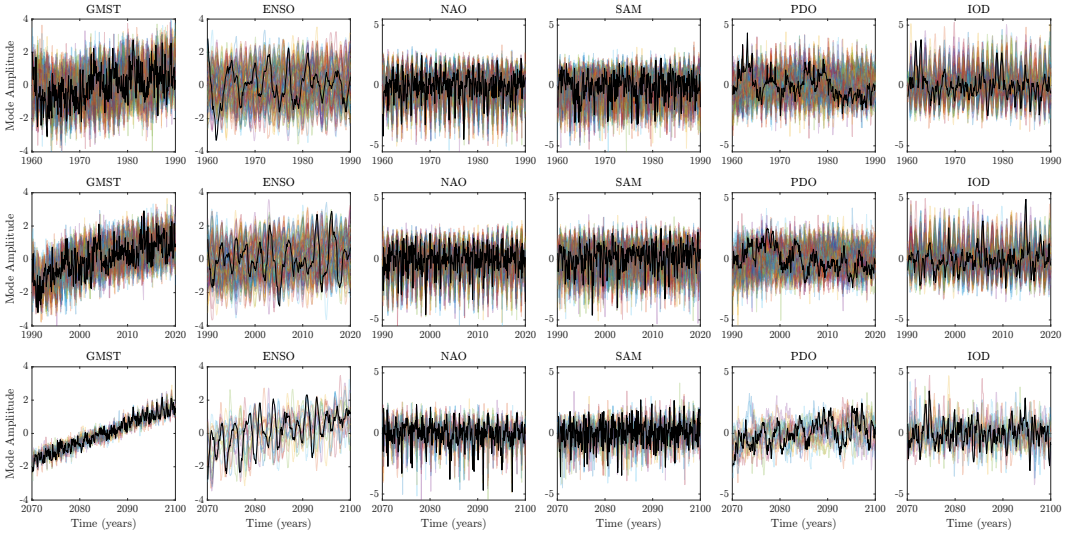

Figure SI9. CESM2-LE internal variability indexes for the period of 1960-1990, 1990-2020, and 2070-2100. The black line represents the internal variability mode index from one run, and the colors are additional runs to show the amplitude range.

Table S1. Correlation matrix between major monthly climate indices.

	GMST	ENSO	NAO	SAM	PDO	IOD
GMST	X	0.2115	-0.0501	0.1354	0.1054	0.2875
ENSO	0.2115	X	-0.0106	-0.1379	0.4694	0.2671
NAO	-0.0501	-0.0106	X	0.0108	-0.0466	-0.0839
SAM	0.1354	-0.1379	0.0108	X	-0.0067	0.0073
PDO	0.1054	0.4694	-0.0466	-0.0067	X	-0.0782
IOD	0.2875	0.2671	-0.0839	0.0073	-0.0782	X

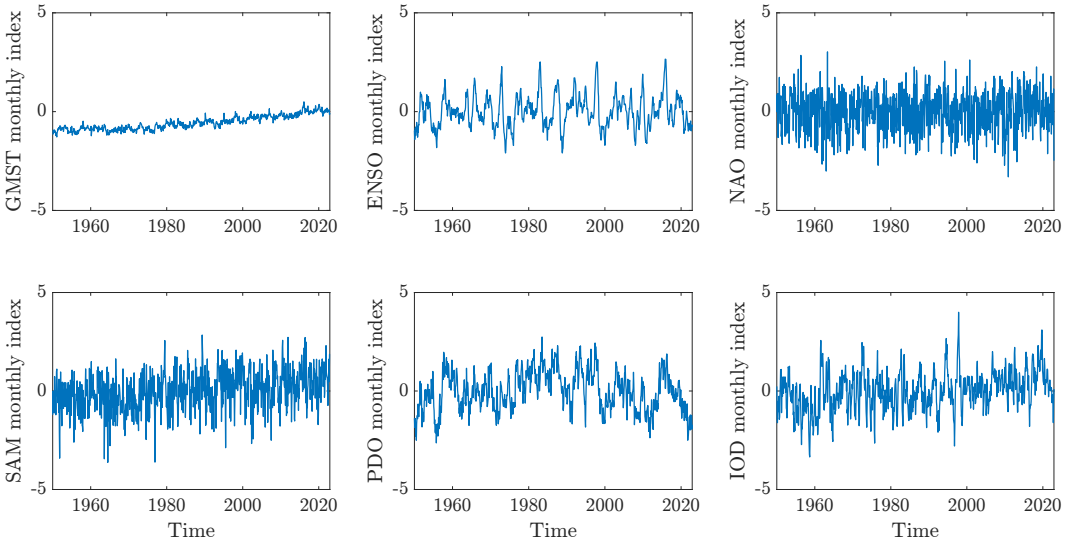

Figure SI10. Observed internal variability indexes for the period of 1950-2020.

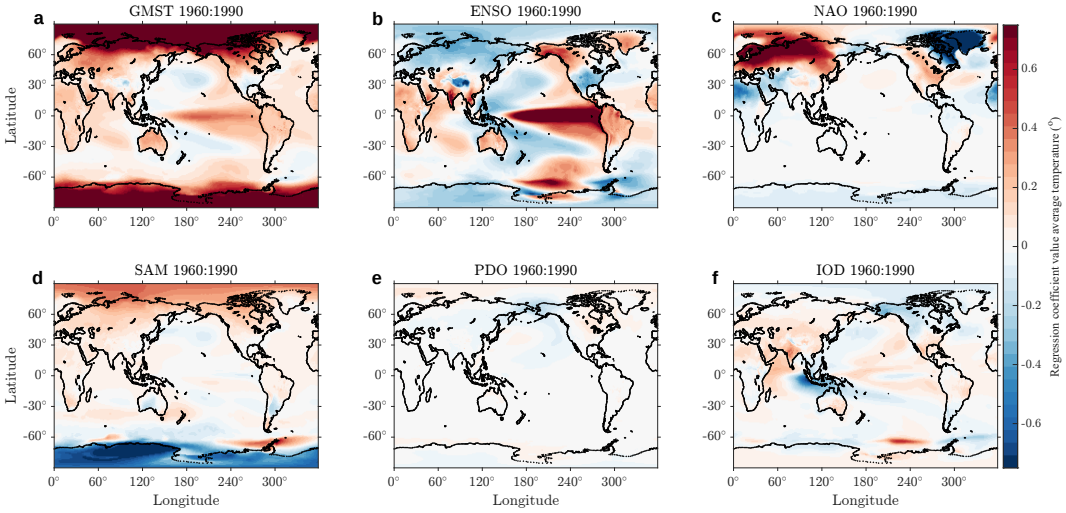

Figure SI11. CESM2-LE regression coefficients mean between standardized and orthogonalized time series for several internal climate variability modes and the local monthly average temperature, calculated for 1960-1990.

Table S2. The variance of internal variability mode indices for the two periods analyzed in the paper.

Period	GMST	ENSO	NAO	SAM	PDO	IOD
1961–1990	0.0316	0.6872	2.9498	0.9950	0.8284	0.1150
1991–2020	0.0597	0.7183	2.9367	0.9950	1.0106	0.1102

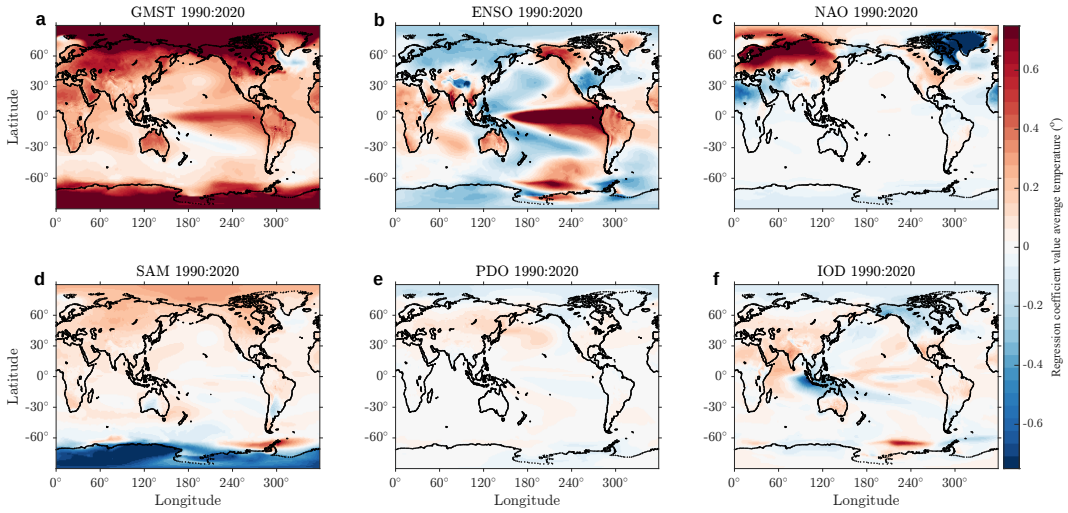

Figure SI12. CESM2-LE regression coefficients mean between standardized and orthogonalized time series for several internal climate variability modes and the local monthly average temperature, calculated for 1990-2020.

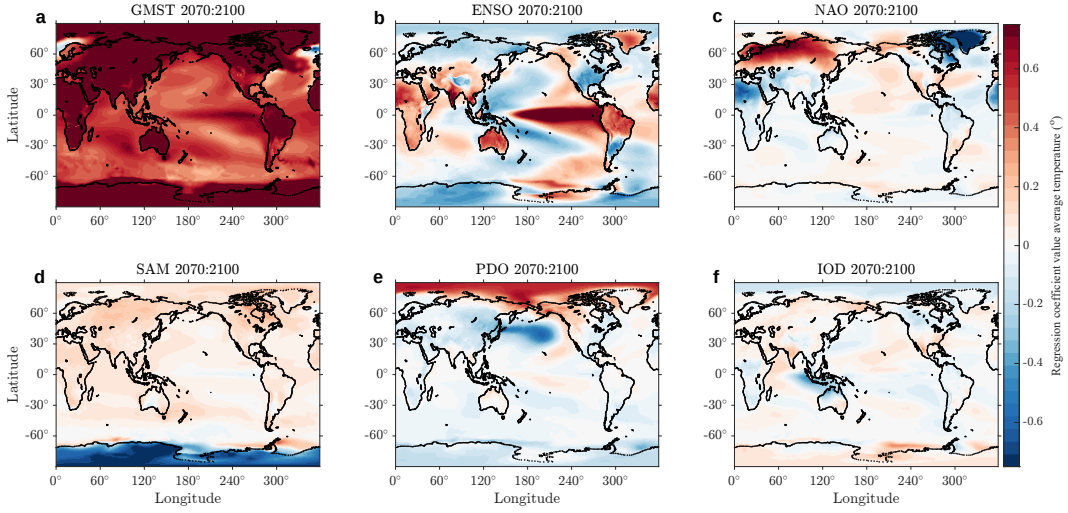

Figure SI13. CESM2-LE regression coefficients mean between standardized and orthogonalized time series for several internal climate variability modes and the local monthly average temperature, calculated for 2070-2100.

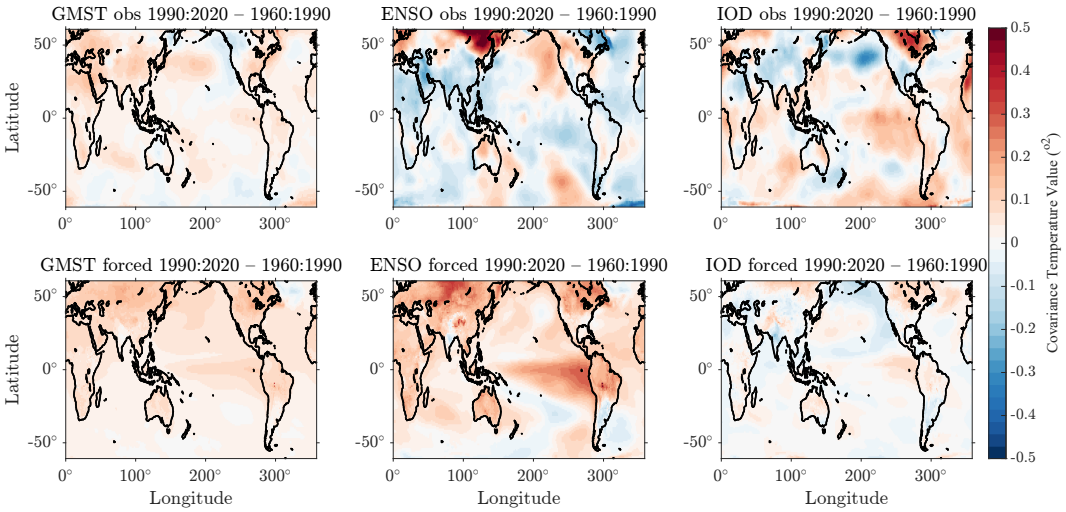

Figure SI14. A comparison of the covariance fingerprinting difference between 1990-2020 and 1960-1990 results between observations and the CESM2-LE historical run ensemble mean, expanded from different regions.

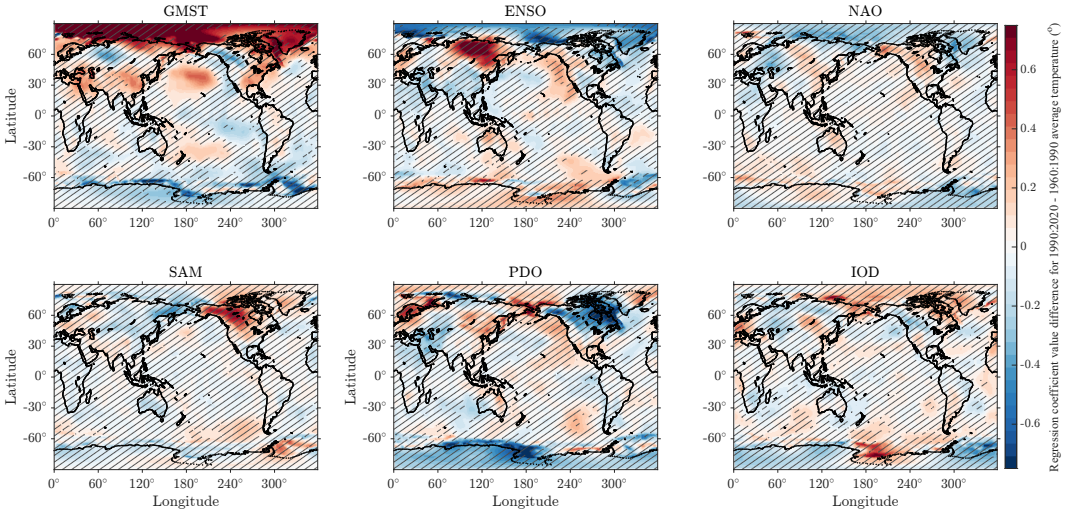

Figure SI15. Same as Fig.3, except here, hatching represents locations where attribution to climate change is not possible.

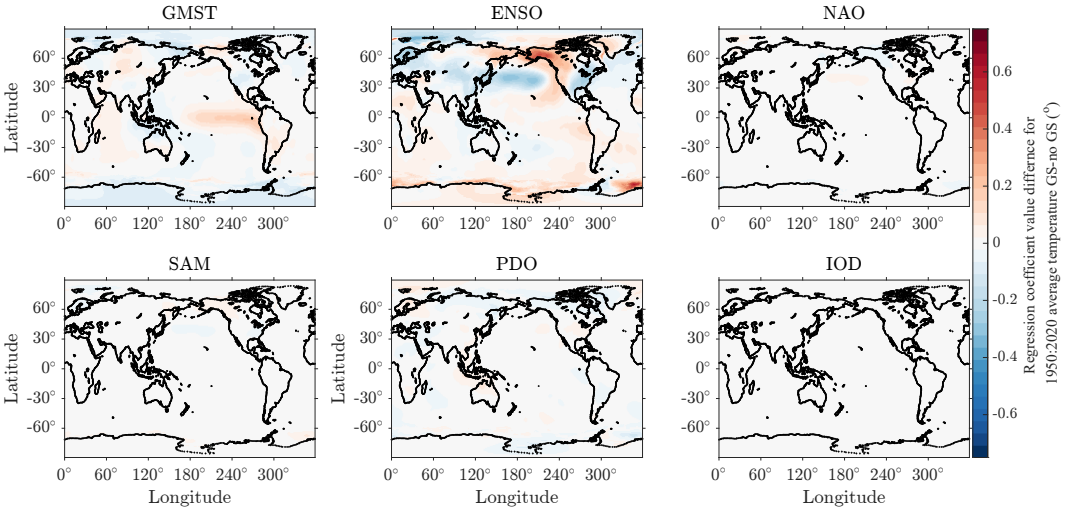

Figure SI16. A comparison of the regression coefficients difference between 1990-2020 and 1960-1990 for a run with Gram-Schmidt orthogonalization to a run without orthogonalization.

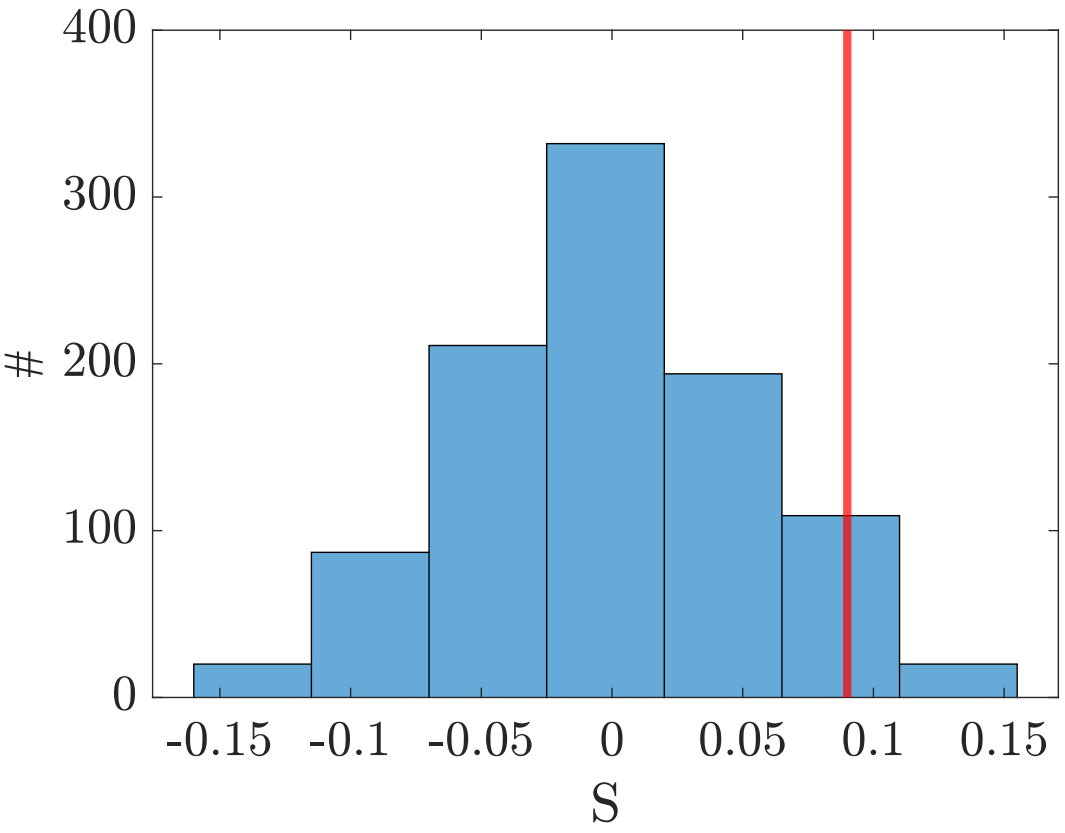

Figure SI17. Same as Figure 2, but using the alternative formulation that is more analogous to a correlation, emphasizing the spatial pattern of covariance changes while being insensitive to their amplitude. The observed scalar S_{obs} (0.09) exceeds the 95th percentile of S_{null}

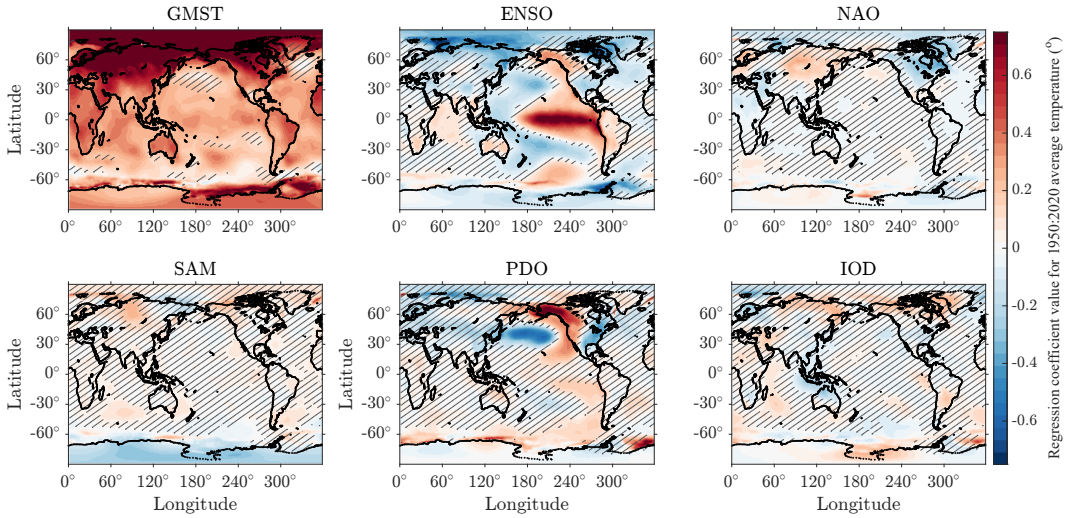

Figure SI18. Same as Fig. SI1, but with bootstrapping performed after randomizing the response variable in the phase diagram.

References

Anderson, W., Seager, R., Baethgen, W., & Cane, M. (2017). Life cycles of agriculturally relevant ENSO teleconnections in North and South America. *International Journal of Climatology*, *37*(8), 3297–3318.

Cai, W., McPhaden, M. J., Grimm, A. M., Rodrigues, R. R., Taschetto, A. S., Garreaud, R. D., ... others (2020). Climate impacts of the El Niño–southern oscillation on South America. *Nature Reviews Earth & Environment*, *1*(4), 215–231.

Cai, W., Van Rensch, P., Cowan, T., & Hendon, H. H. (2011). Teleconnection pathways of ENSO and the IOD and the mechanisms for impacts on Australian rainfall. *Journal of Climate*, *24*(15), 3910–3923.

Danabasoglu, G., Lamarque, J.-F., Bacmeister, J., Bailey, D. A., DuVivier, A. K., Edwards, J., ... Strand, W. G. (2020). The Community Earth System Model Version 2 (CESM2). *Journal of Advances in Modeling Earth Systems*, *12*(2), e2019MS001916. doi: https://doi.org/10.1029/2019MS001916

Hou, Y., Xie, S.-P., Johnson, N. C., Wang, C., Yoo, C., Deng, K., ... Li, X. (2024). Unveiling the indian ocean forcing on winter eastern warming–western cooling pattern over north america. *Nature Communications*, *15*(1), 9654.

Hurrell, J. W. (1995). Decadal trends in the north atlantic oscillation: Regional temperatures and precipitation. *Science*, *269*(5224), 676–679.

Kay, J. E., Deser, C., Phillips, A., Mai, A., Hannay, C., Strand, G., ... others (2015). The Community Earth System Model (CESM) large ensemble project: A community resource for studying climate change in the presence of internal climate variability. *Bulletin of the American Meteorological Society*, *96*(8), 1333–1349.

Kumar, K. N., Molini, A., Ouarda, T. B., & Rajeevan, M. N. (2017). North Atlantic controls on wintertime warm extremes and aridification trends in the Middle East. *Scientific Reports*, *7*(1), 12301.

Linderholm, H. W., Ou, T., Jeong, J.-H., Folland, C. K., Gong, D., Liu, H., ... Chen, D. (2011). Interannual teleconnections between the summer North Atlantic Oscillation and the East Asian summer monsoon. *Journal of Geophysical Research: Atmospheres*, *116*(D13).

Mantua, N. J., Hare, S. R., Zhang, Y., Wallace, J. M., & Francis, R. C. (1997). A pacific interdecadal climate oscillation with impacts on salmon production. *Bulletin of the american Meteorological Society*, *78*(6), 1069–1080.

Marshall, G. J. (2003). Trends in the southern annular mode from observations and reanalyses. *Journal of climate*, *16*(24), 4134–4143.

Montgomery, D. C., Peck, E. A., & Vining, G. G. (2021). *Introduction to linear regression analysis*. John Wiley & Sons.

North, G. R., Bell, T. L., Cahalan, R. F., & Moeng, F. J. (1982). Sampling errors in the estimation of empirical orthogonal functions. *Monthly weather review*, *110*(7), 699–706.

Roy, I., Tedeschi, R., & Collins, M. (2016). ENSO teleconnections to the Indian summer monsoon in observations and models. *International Journal of Climatology*.

Saji, N., Ambrizzi, T., & Ferraz, S. E. T. (2005). Indian Ocean Dipole mode events and austral surface air temperature anomalies. *Dynamics of atmospheres and oceans*, *39*(1-2), 87–101.

Saji, N., Goswami, B. N., Vinayachandran, P., & Yamagata, T. (1999). A dipole mode in the tropical indian ocean. *Nature*, *401*(6751), 360–363.

Sandler, D., Saaroni, H., Ziv, B., Tamarin-Brodsky, T., & Harnik, N. (2024). The connection between North Atlantic storm track regimes and eastern Mediterranean cyclonic activity. *Weather and Climate Dynamics*, *5*(3), 1103–1116.

Shi, N., Tian, P., & Zhang, L. (2019). Simultaneous influence of the Southern Hemisphere annular mode on the atmospheric circulation of the Northern Hemisphere during the boreal winter. *International Journal of Climatology*, *39*(5), 2685–2696.

Thompson, D. W., & Wallace, J. M. (2000). Annular modes in the extratropical circulation. part i: Month-to-month variability. *Journal of climate*, *13*(5), 1000–1016.

Yang, X., & DelSole, T. (2012). Systematic comparison of ENSO teleconnection patterns between models and observations. *Journal of climate*, *25*(2), 425–446.

Zhou, L., Hua, W., Nicholson, S. E., & Clark, J. P. (2024). Interannual teleconnections in the Sahara temperatures associated with the North Atlantic Oscillation (NAO) during boreal winter. *Climate Dynamics*, *62*(2), 1123–1143.